UNIVERSITY OF OKLAHOMA

GRADUATE COLLEGE

EFFECTS OF MASS WASTING ON FLUVIAL SEDIMENTS IN PUERTO RICO FOLLOWING HURRICANE MARIA

A THESIS

SUBMITTED TO THE GRADUATE FACULTY

In partial fulfillment of the requirements for the

Degree of

MASTER OF SCIENCE

By

NINA DANIELLE SZABO WEBB

Norman, Oklahoma

2020

EFFECTS OF MASS WASTING ON FLUVIAL SEDIMENTS IN PUERTO RICO FOLLOWING HURRICANE MARIA

A THESIS APPROVED FOR THE
SCHOOL OF GEOSCIENCES

BY THE COMMITTEE CONSISTING OF

Dr. Megan E. Elwood Madden, Chair

Dr. Andrew S. Elwood Madden

Dr. Netra Regmi

Dr. Gerilyn S. Soreghan

Dedicated with love to

my

Grandparents

ACKNOWLEDGEMENTS

I would like to thank the University of Oklahoma for the incredible opportunity to receive a remarkable education and work with some amazing minds.

I am forever grateful to Dr. Megan E. Elwood Madden for her unending support, guidance, patience, and kindness. The opportunities you afforded me are priceless and I will forever cherish the research I was blessed to be a part of. Thank you to my committee for your support and guidance through this research journey. Your expertise and teaching have helped me to discover how to do the best research possible.

Many thanks to my field partners Jordan Sylvester and Fabiola M. Cartagena Colon for an amazing experience. Thank you to my lab mates, specifically Cansu Floyd, for sharing knowledge and helping with many hours of sample processing and Dr. Charity Phillips-Lander for your support in and out of the lab.

To my love, Forrest, for always making sure I had sustenance and for all of your love and support. Theresa, thank you for countless edits and always pushing me to succeed. Joy, for always acting interested even when you had no idea what I was talking about. Uncle Kyle and Aunt Christy, for always being there for support in every way possible. Kevin, for being the best Dad you know how to be. AJ for being there for me when needed.

TABLE OF CONTENTS

Page

Abstract

Mass wasting can supply abundant sediment to fluvial systems, but the effects on carbon cycling and chemical weathering signatures in fluvial sediments are ambiguous. Here we examine the impacts of mass wasting on sediment delivered to the fluvial systems in high relief and high precipitation watersheds in southeastern Puerto Rico to investigate the role of hurricane-induced mass wasting on carbon cycling and fluvial sediment properties. Previous work hypothesized that anomalously low chemical index of alteration (CIA) values observed in fluvial sediment in these watersheds were a result of landslides delivering less weathered regolith to the Rio Guayanés and Rio Guayabo. On September 20, 2019, Hurricane Maria made landfall in Puerto Rico, resulting in thousands of landslides across the island and an opportunity to examine this hypothesis. However, the sediments collected after the hurricane-induced landslides have higher weathering index values and coarser-grain sizes than those collected in 2014. We infer that the heavy precipitation associated with Hurricane Maria led to the mass movement of weathered topsoil and saprolite in relatively shallow landslides as opposed to deep seated landslides sampling bedrock. The exposure of fresh bedrock via landslide scarps and the deposition of sediment on hillslopes and within the fluvial system may play an important role in carbon sequestration. The variances in CIA values observed are not indicative of the degree of climate change, but instead are likely due to subtle differences in transport mechanism which can lead to significant differences in the weathering index values.

Introduction

Weathering trends are important to understand as they affect both the short and long-term carbon cycles as well as serve as paleoclimate proxies (White et al., 1998, 1999). Increased mass wasting due to climate - and land - use change may increase chemical weathering rates (Moore et al., 2019; Oliva et al., 2003), resulting in consumption of carbon dioxide and providing a slight negative feedback effect for global warming, as well as affecting stream quality and ecology (Sassa & Canuti, 2009). However, the full effect of mass wasting on the carbon cycle is unclear (Buss et al., 2017; Emberson et al., 2018; Oliva et al., 2003).

Carbon sequestration is observed in regions where physical weathering and rapid chemical weathering of silicates occurs (Gaillardet et al., 1999). According to Fernandes et al. (2016), chemical weathering of fresh bedrock delivers cations into fluvial systems and is a primary consumer of CO_2 from Earth's atmosphere. However, Emberson et al. (2018) found that landslides tend to be a net source for CO_2 to the atmosphere when they expose carbonate and sulfide minerals to weathering. This suggests that the type of bedrock that is exposed and weathered plays an important role in determining if carbon is sequestered or released to the atmosphere.

The relative size of the landslides also likely plays an important factor in determining the degree of weathering observed in the sediment delivered to the fluvial system. For example, deep-seated landslides that sample bedrock deliver much less weathered sediment versus shallow landslides which deliver highly weathered saprolite and/or soils (Bessette-Kirton et al., 2019). The slope stability of a region contributes to the size and frequency of landslides (Bessette-Kirton et al., 2019; Varnes, 1978). Factors that can predispose hillslopes to landslides include hillslope morphology (i.e. slope, curvature, etc.), geology and soil; the factors that can trigger

landslides are precipitation events, earthquakes, and anthropogenic activities (Lehmann et al., 2013; Varnes, 1978). Therefore, the nature of the underlying bedrock plays an important role in determining not only the rate of weathering, but also the size of possible landslides and if carbon is sequestered. Increasing precipitation and tropical storms associated with rising global temperatures implies an increase in the number of mass wasting events (Crozier, 2010), as well as, potentially, the volume of landslides. Regional tectonics also has a direct influence on the slope of the terrain and can lead to slope instability, particularly in the event of intense and prolonged precipitation which can be correlated with mass wasting events (Aristizábal et al., 2005; Caine, 1980; Lehmann et al., 2013).

The impact of mass wasting on the weathering indices of sediment delivered to streams located in high relief and high precipitation localities has not been clearly determined, and may provide important evidence of historical weathering trends, or could predict future trends likely to occur with future landslides (Bluth & Kump, 1994; Joo et al., 2018). Mass wasting introduces a range of sediment grain sizes to fluvial systems (Larsen & Torres-Sánchez, 1998). However, the grain size distribution of sediments delivered to fluvial systems can also be influenced by several other factors, including 1) bedrock lithology (Roda-Boluda et al., 2018); 2) chemical weathering processes, particularly in tropical regions where more weathering leads to finer grain sizes (Fernandes et al., 2016); 3) transport mechanisms, where landslides and glaciers tend to result in poorly sorted, coarse-grained sediment delivered to the fluvial systems compared to overland flow and stream transport which result in more sorting and deposition of finer sediment (Roda-Boluda et al., 2018).

In the absence of steep slopes, sediment is weathered over a longer period of time and is eventually transported into the fluvial system through overland flow. The sediment supplied

from gradual erosion of soil to the fluvial system is finer grained and more homogeneous (ie. well-sorted) (Attal et al., 2015), while sediment supplied from landslides is coarser, poorly sorted, and can result in sediment grain sizes coarsening downstream when associated with heavy precipitation events, compared to the general trend of distal fining expected in a typical fluvial system (Attal et al., 2015; Roda-Boluda et al., 2018; Struck et al., 2015).

Due to stochastic events, such as mass wasting, fluvial sediment properties can vary widely. Anomalously low chemical index of alteration (CIA) values observed in fluvial sediments collected from a granitic watershed in Puerto Rico in 2014 have been previously attributed to mass wasting (Joo et al. 2018). Joo et al. posited that since the sediment within the fluvial system is less weathered than expected for the climate regime, this may indicate that the sediment was derived from bedrock sampled by deep-seated or large landslides triggered by hurricanes. Hurricane Maria (September 20th, 2017) initiated widespread mass wasting in the study area (Bessette-Kirton et al., 2019; Keellings & Hernández Ayala, 2019; Ramos-Scharrón & Arima, 2019); this event thus provided the opportunity to directly observe the impact of hurricane-induced mass wasting on fluvial sediments and test if Joo et al.'s predictions were correct. If the predictions were correct, we expected to observe larger grain sizes, a decrease in surface area, and lower CIA values indicative of less intense weathering in the fluvial sediments collected post-Maria, since they had recently been impacted by hurricane-induced landslides.

Steep slopes in humid climates with abundant precipitation are less stable and more prone to mass wasting events such as landslides versus arid climates (Gariano & Guzzetti, 2016; Shiels & Walker, 2013). Joo et al. (2018) predict that mass wasting events supply the fluvial system with larger grains that are less weathered and derived from bedrock, regolith, or saprolite rather than soils. Additionally, they predicted that mass wasting would deliver not only larger grain

sizes than systems without mass wasting events , but also a wider range of grain sizes and less weathered grains (Attal et al., 2015; Hubert & Filipov, 1989). This study aims to investigate the impact of mass wasting on fluvial sediment properties as well as bridge the gap between these properties and chemical weathering indices to analyze potential impacts on climate change.

Background

Geology

Puerto Rico, located in the Caribbean Sea southeast of Florida, consists of Jurassic to Eocene igneous bedrock (Monroe, 1980). The study region, located in the southeastern part of the island, is characterized by normal faults. Rio Guayabo and Rio Guayanés follow these normal faults through the Cordillera Central Mountain range. Both fluvial systems are underlain by the Late Cretaceous San Lorenzo granodiorite (Rogers et al., 1979). The granodiorite is overlain by saprolite ranging from approximately 2-8m thick and then 0.5-1m of soil, according to other similar study regions in Puerto Rico (Fletcher et al., 2006; Murphy et al., 2012). The regional tectonic system is characterized by left-lateral slip deformation along the Puerto Rico Trench (Masson & Scanlo, 1991), resulting in moderate earthquake activity.

Climate and Land Usage

The average annual temperature for Yabucoa, (a town directly east of the study region) is 25˚C with an average annual rainfall of 4000 mm and approximately one hurricane every two years (Larsen, 2000; Lepore et al., 2012). The land in the study region is subtropical wet forests and sparsely populated rural areas where agricultural land use declined by ninety-five percent from 1951 to 2000 (Birdsey & Weaver, 1982; Martinuzzi et al., 2007). During the 16th century, European settlers began massive deforestation efforts to support agriculture, resulting in the destruction of the majority of mature forests by the 19th century (Birdsey & Weaver, 1982). Until the 1940s, sugar cane was the main source of income and thus, all but 3400 hectares of land was deforested, with regional forest only returning since the 1950s as a result of abandonment of small farms (Birdsey & Weaver, 1982). More recent anthropogenic forcings in the form of road construction increases deforestation and decreases slope instability with the

highest density of landslides in Puerto Rice occurring within 85 m of roads (Larsen & Parks, 1997).

Mass wasting

Landslides are one of many types of mass wasting processes that commonly occur in mountainous terrains and pose a major hazard that results in loss of life and property in Puerto Rico (Bessette-Kirton et al., 2019; Dou et al., 2015; Keellings & Hernández Ayala, 2019; Lepore et al., 2012). Lepore et al. (2012) conducted a landslide susceptibility assessment of various areas in Puerto Rico and projected high to very high risk owing in part to the bedrock lithology (Bessette-Kirton et al., 2019). The severe deforestation along with steep slopes and high annual rates of precipitation observed in Puerto Rico results in higher rates of erosion (Birdsey & Weaver, 1982). Similarly, earthquakes can also trigger mass wasting events; however, this is largely dependent on soil saturation in conjunction with seismic activity as well as bedrock lithology (Bessette-Kirton et al., 2019; Reid & Taber, 1918).

Fluvial Systems

The two fluvial systems that we sampled are the Rio Guayanés to the north and the Rio Guayabo in the south. The Rio Guayanés watershed is 23.24 km^2 with a minimum elevation of 20.5 m and maximum elevation of 539 m above sea level. The Rio Guayabo watershed is 8.53 km^2 with a minimum elevation of 23.3 m and maximum elevation of 497.4 m above sea level.

Chemical weathering indices

Chemical weathering is strongly related to lithology and climate. Chemical weathering tends to be more intense in tropical mountainous environments where runoff is present (Oliva et al., 2003). The chemical index of alteration, or CIA, is an indicator of the chemical weathering of feldspars to clays (Goldberg & Humayun, 2010). The CIA values of fluvial muds have been

quantified for some subtropical and tropical areas and are often used as a proxy for paleoclimate interpretation (Nesbitt & Young, 1982). The weathering of feldspars results in the removal of mobile cations such as calcium, potassium, and sodium which leads to an increase in the proportion of Al_2O_3 in the fluvial mud (Aristizábal et al., 2005; Nesbitt & Young, 1982). High CIA values (>90) are indicative of extensively weathered soil depleted in calcium and sodium and enriched in aluminum (Nesbitt & Young, 1982). This removal of mobile cations can be measured with CIA to determine the amount of weathering and is calculated using the following formula from Nesbitt and Young, 1982.

$$Eq.1 \qquad CIA = \left[\frac{Al_2O_3}{(Al_2O_3 + CaO^* + Na_2O + K_2O)}\right] x\ 100$$

The CIA value for fluvial mud in the tropical study area of Puerto Rico was abnormally low (58-69) in 2014 compared to expected values (>90), considering Puerto Rico is subject to some of the highest weathering rates in the world and has a tropical-subtropical climate (Joo et al., 2018; White et al., 1998; White & Blum, 1995).

Variations in cations in sediments relative to bedrock composition also provides an indication of the degree of weathering of the sediment within the study area. The concentration of CaO, Na_2O, MgO, and Fe_2O_3 in the mud decreased distally, while K_2O increased distally (Joo et al., 2018), suggesting that the degree of chemical weathering observed in the sediments increases downstream, perhaps due to preferential transport of clays.

An alternative multicomponent weathering index developed by Ohta & Arai (2007) uses principal component analysis to determine the degree of weathering of the mud size fraction. This principle component method uses wt % SiO_2, TiO_2, Al_2O_3, Fe_2O_3, MgO, CaO, Na_2O, and K_2O to describe chemical weathering trends in diverse bedrock lithologies (Ohta & Arai, 2007). Principal component analysis uses the provided variables to produce new orthogonal

components, or principal components, that are uncorrelated to one another, but capture as much of the original variance within the dataset provided for analysis. Using principal component analysis encompasses the behavior of multiple elements, as well as assuming normally distributed geochemical variability typically found in fresh mafic, fresh felsic, and weathered rock (Ohta & Arai, 2007). The derived principal components can then be mapped on a ternary diagram (much like CIA values can be plotted in Ca+Na-Al-K space), with vertices *MFW*, where the *M* and *F* represent the mafic and felsic portion of the rock source, and *W* represents the degree of weathering of the mafic and felsic portions, independent of the parent rock source, based on the eight oxide variables above (Ohta & Arai, 2007). The following equations are from a multicomponent linear regression from Ohta & Arai, 2007:

$$Eq.2 \quad M = -0.395 \times ln(SiO_2) + 0.206 \times ln(TiO_2) - 0.316 \times ln(Al_2O_3) + 0.160 \times ln(Fe_2O_3) + 0.246 \times ln(MgO) + 0.368 \times ln(CaO^*) + 0.073 \times ln(Na_2O) - 0.342 \times ln(K_2O) + 2.266$$

$$Eq.3 \quad F = 0.191 \times ln(SiO_2) - 0.397 \times ln(TiO_2) + 0.020 \times ln(Al_2O_3) - 0.375 \times ln(Fe_2O_3) - 0.243 \times ln(MgO) + 0.079 \times ln(CaO^*) + 0.392 \times ln(Na_2O) + 0.333 \times ln(K_2O) - 0.892$$

$$Eq.4 \quad W = 0.203 \times ln(SiO_2) + 0.191 \times ln(TiO_2) + 0.296 \times ln(Al_2O_3) + 0.215 \times ln(Fe_2O_3) - 0.002 \times ln(MgO) - 0.448 \times ln(CaO^*) - 0.464 \times ln(Na_2O) + 0.008 \times ln(K_2O) - 1.374$$

Methods

Fluvial sediment, saprolite, and stream water samples were collected from the Rio Guayanés and Rio Guayabo in the southeastern portion of Puerto Rico in June 2018 nine months post Hurricane Maria using GPS locations to ensure similar localities to Joo et al. (2018). The fine-grained sediment was obtained from the slack water areas of fluvial bars at intervals ranging from ~1-5 km between sampling points, beginning at the upland source of the stream and continuing~21 km in total distance downstream. Saprolite samples were obtained within the study region as it was observed along roadcuts. Sediment and water samples were frozen upon returning to the lab and prior to analyses.

Landslide Mapping

We used 10 m by 10 m LiDAR topographic data and 1/3 arc-second USGS NED digital elevation models (DEMs) (USGS National Map, 2020) to quantify the landslides in southeastern Puerto Rico. Using the spatial analysis tool, the images were merged together by applying the mosaic tool in Python and ArcGIS®. We used aerial photographs from Google Earth® and LiDAR DEM-based hillshade relief map to identify and map landslides that occurred pre- and post- Hurricane Maria along both fluvial systems (USGS National Map, 2020). A hydrologic geoprocessing model was applied to both the 1 m and 10 m DEMs to extract the hydrological network. The area of the mapped landslides was calculated using the geometry calculation tool in ArcGIS® which was then used to determine the minimum, mean, and maximum landslide areas. Volume was calculated using the following equation from Regmi et al. (2014), where V and A represent volume and area, repectively:

$$Eq.5 \quad V = 0.0254 * A^{1.45}$$

This equation was used as an accurate representation of volume when applied to shallow landslides and is not significantly different from the equations proposed for volume calculation of shallow landslides in various parts of the world (Regmi et al., 2014; Tron et al., 2014). Additionally, this equation has been successfully employed in regions with similar lithology and topography were noted to the Puerto Rico landslides.

A probability distribution of the mapped landslides was calculated using the Gaussian kernel density method to determine the probability density function (Silverman, 1984). This non-parametric method of estimation, using the number of landslides within an area, provides information about the probability of occurence of different sized landslides. A spatial density map was constructed using kernel density estimation with ArcGIS® to represent the density of landslide occurrence (Guzzetti et al., 2008).

Grain size analysis

All samples were wet sieved to obtain different size fractions of gravel (>2 mm), sand (63 μm – 2 mm), and mud (<63 μm), then the mud was treated with buffered acetic acid and hydrogen peroxide to remove carbonates and organic matter, respectively. After the mud samples were treated, a small portion was set aside in a glass vial for laser particle size analysis. Three to five drops of sodium metaphosphate, a liquid dispersant, was added to all mud samples before the samples were placed in an ultrasonic bath to agitate the particles for ~ thirty seconds. The samples were then analyzed promptly using a Malvern Mastersizer 3000 laser particle size analyzer (LPSA) in a liquid dispersion unit. The mud samples consist of various size fractions, all < 63 μm (Malvern, 1997). Resulting LPSA measurements were used to compare the relative grain size of the mud fraction in 2018 versus 2014. Utilizing LPSA, particle size metrics such as span, kurtosis, uniformity, and skewness can be derived from the mud size fraction of fluvial

sediment to provide information on sorting and grain size, in addition to other information (Liu et al., 1966).

Mineralogy and surface area

The remaining treated mud samples were freeze dried prior to specific surface area (SSA) analysis using the six-point BET (Brunauer-Emmett-Teller) nitrogen adsorption isotherm (Brunauer et al., 1938). The mud samples were passed through a fine-grained sieve to separate any clumps in preparation for a random mount on a glass slide for powder X-ray diffraction (XRD) analysis. We filled a shallow well in a glass slide using a spatula to ensure that the mud sample was level with the top of the slide but without compacting the sample and applying minimum pressure to ensure near-random orientation (Harris, W., & White, 2008). These random mounted samples were analyzed using the Rigaku Ultima IV diffractometer using Cu-K-alpha radiation at 40 kV and 44 mA. We used the Bragg-Brentano method with a range of 2-70° 2θ at 0.02° step size. Resulting diffraction patterns were analyzed with MDI JADE Pro software by whole pattern fitting for bulk mineral identification.

Bulk geochemical analysis and chemical weathering indices

A portion (~3-3.5 g) of the processed mud was sent to ALS, where the solid samples were dissolved in strong acid and analyzed using inductively coupled plasma-atomic emission spectrometry (ICP-AES). In a few cases, the samples were too small to be measured on their own, so we added a known portion of corundum standard and later corrected for the added Al_2O_3 in the geochemistry results.

The CIA values of the mud fraction of the fluvial sediment were then calculated using the formula from Nesbitt and Young (1982). The resulting data were plotted on a ternary diagram with vertices of $CaO+Na_2O$, K_2O, and Al_2O_3 with more weathered samples plotting towards the

Al_2O_3 vertex. Using the PCA data developed by Ohta and Arai (2007), an alternative chemical weathering index was also computed based on the bulk chemistry data and plotted on a ternary diagram with vertices of M, F, and W with more weathered samples plotting towards the W vertex.

Water chemistry

Water samples collected in the field were filtered through a 0.22 µm filter using a Millipore vacuum system, treated with 1M hydrochloric acid and frozen. The samples were then sent to the Oklahoma State University Soil, Water and Forage Analytical Laboratory where the samples were analyzed using inductively coupled plasma-optical emission spectrometry (ICP-OES). The resulting data were used to plot aqueous cation concentration versus distance downstream to analyze chemical weathering solutes released from the sediment within the fluvial system.

Results

Mass Wasting

We identified 116 landslides that occurred within ~350 m from the study trunk streams during the eight-month period following Hurricane Maria. The average area of the 116 mapped landslides was 238 m^2, ranging from a minimum of 11 m^2, to a maximum of 2230 m^2 (Table 1). The average modeled volume of the mapped landslides is ~110 m^3, and the average depth of the landslides is computed as ~0.25 m by taking the ratio of volume to area (Table 1 & A2). The probability density function plot (Fig. 1) suggests that most of the observed landslides are relatively small. The landslides are observed to occur at all slopes within the study region with the highest proportion occurring at ~24-26˚, which also correlates to the most prevalent slopes in the area (Fig. 2). The average slope of both the landscape and the locations where landslides occur, is 19.6˚ with a standard deviation of 9.3 and 10.6, respectively (Fig. 2).

Using kernel density estimation with a 1 km^2 circular neighborhood, a spatial density map of the landslides was created (Fig. 3). The highest density of landslides is observed between samples five and seven along Rio Guayanés and between three and four of the Rio Guayabo (Fig. 3). The clustering of landslides can provide information regarding the terrain and slope stability of an area (Miller & Burnett, 2007; Schulz, 2007).

Rio Guayanés Sediment – Sieved grain size fraction

The weight percent of sand is much higher (~75 wt%), than the weight percent of mud (<20 wt%) for samples collected in both 2014 and 2018 (Fig. 4B, C). However, both the sand and mud display a wider range of variability for the post-hurricane sample set, with the weight percent of mud generally higher post Hurricane Maria in the most proximal and distal portions of the stream compared to pre-Hurricane Maria (Fig. 4B, C). The weight percent of gravel is much

lower in the 2018 samples post-hurricane compared with the 2014 samples, with the exception of the most proximal sample location and sample eight (Fig. 4A).

The trends in weight percent of clay-sized grains (Fig. 4D) in the 2014 and 2018 sample sets are opposite: a higher concentration of clay-sized grains was observed in distal samples in 2014 whereas, in 2018, higher weight percents of clay occur in the more proximal samples (Fig. 4D). The silt displays similar trends but higher weight percent in 2018 compared to 2014 with the second to last distal sample having a much greater amount of silt (Fig. 4D). Opposite trends in grain size mode were also observed in the 2018 samples which increased with distance downstream, whereas the grain size mode generally decreased with distance downstream in the 2014 samples (Fig. 5). The mud in the 2018 samples consists primarily of silt sized grains (4-63 μm) in all samples with the exception of PM-RG-SED-3 which has a nearly evenly bimodal distribution of silt and clay (<4 μm) (Fig. A.1). All other samples exhibit a left-skewed (coarser) distribution (Fig. A.1).

Proximal

Overall, the sediment in the most proximal samples is coarser grained in 2018 compared to 2014. While the weight percent of gravel was lower in 2018 compared to 2014 (Fig. 4A, B, C), the clay fraction is also generally lower in the proximal 2018 samples, with the exception of the third sample location (Fig. 4D). The amount of sand observed is slightly higher in 2018, post Hurricane Maria. The overall mud-sized sediment fraction observed in samples collected pre-Hurricane Maria (2014) did not change significantly between the first seven proximal samples (Fig. 4C). However, more silt was observed proximally in 2018 than in 2014 (Fig. 4D). The clay size fraction in 2018 is virtually nonexistent and the silt and clay within the mud size fractions in

2018 have very similar trends (Fig. 4C & D). More variation was observed overall in the different size fractions in 2018 than in 2014 (Fig. 4).

Mid-Stream

The weight percent of gravel observed in the samples collected from the mid portion of the stream (samples 4-7) was much lower in 2018 than in 2014, while the weight percent of both sand and silt are generally higher in the 2018 samples (Fig. 4A, B). The mud, as well as clay and silt within the mud, trends are comparable in both 2014 and 2018 (Fig. 4C, D).

Distal

The most distal samples (8-10), illustrate opposite weight percent trends in gravel from 2014 and 2018, with higher gravel concentrations observed distally in 2014 (Fig. 4A), while the sand, mud, and silt/clay within the mud, fractions display similar trends in both 2014 and 2018 (Fig. 4B &D).

Rio Guayanés Sediment - Mineralogy and Bulk Chemistry

The mud size fraction collected in 2018 consists of mainly albite, quartz, amphibole, clay minerals, and mica (Table A.1). No systematic change in mineralogy was observed from proximal to distal samples within the Rio Guayanés fluvial system in the 2018 samples. The 2014 samples exhibited a general distal decrease of primary minerals (quartz, plagioclase, hornblende, and K-feldspar) in 2014 (Joo et al., 2018).

Rio Guayanés Sediment - Chemical Weathering Indexes

CIA values provide an indication of how weathered the sediment is and are commonly plotted on a ternary diagram to illustrate the removal of the various cations. The Rio Guayanés 2018 sediment CIA values indicate a higher degree of weathering, ranging from 66-88 compared to 58-69 in 2014 (Fig. 7). The average CIA values of the 2018 sediment is nearly 80 while the

average value observed in the 2014 sediment is ~65 (Fig. 8). Similar to the CIA values, the 2018 Rio Guayanés sediment MFW values indicate the sediment is more weathered when compared to 2014 samples (Fig. 9) (Joo et al., 2018).

As the surface area of sediment increases, CIA values are also expected to increase since finer grained sediment fractions have a higher surface area available for weathering and are also more likely to contain clay minerals (White et al., 1996). While this trend is strongly observed in the 2014 Rio Guayanés sediment samples (Fig. 6C, D), only a slight relationship is observed in the 2018 Rio Guayanés sediment (Fig. 6A, B).

Rio Guayabo Sediment - Sieved grain size fraction

Sand is the most abundant grain size fraction in the Rio Guayabo fluvial sediment samples (Fig. 9). The mud size fraction consists primarily of silt sized grains (4-63μm) with a strongly left-skewed (relatively coarse) distribution (Fig. A.3).

Rio Guayabo sediment - BET

The surface area in the Rio Guayabo in the 2018 sediment illustrates very little variability among the four sampling locations (Fig. 11). In the 2014 samples, there is higher surface area in the proximal samples and then the surface area decreases distally, reaching values similar to those observed throughout the 2018 samples (Fig. 11, A.4).

Rio Guayabo sediment - Mineralogy and Bulk Chemistry

The mud size fraction consists of mainly albite followed by clays and amphiboles (Table A.1). Similar to the Rio Guayanés samples, no systematic change in mineralogy was observed from proximal to distal samples within the Rio Guayabo fluvial system.

Rio Guayabo sediment - Chemical Weathering Indexes

The Rio Guayabo CIA sediment values range from 70-81, which plots in the middle of the range of values observed in the Rio Guayanés sediment samples (Fig. 7). The average CIA value of the 2018 Rio Guayabo sediment is 76 while the 2014 sediment average is only slightly lower at 73 (Fig. 8). Comparing the specific surface area with CIA produced very similar trends (Fig. 11). The Rio Guayabo MFW plot (Fig. 12) also indicates more weathered sediment in 2018 compared to 2014 as the sediment samples trend towards the weathered vertex.

Rio Guayanés Saprolite - Sieved grain size fraction

The grain size distributions observed in the Rio Guayanés saprolite samples are highly variable, with some trends observed from proximal (coarser) to distal (finer) along the stream path (Fig. A.5). The mud size fraction of the saprolite contains primarily coarse grains, as seen in the left skewed distribution, but not as coarse as the fluvial sediment (Fig. A.2).

Rio Guayanés Saprolite - BET

The specific surface area of the mud component of the saprolite samples increases proximally and then decreases until the most distal sample which shows variable surface area values for separate samples collected within the same outcrop (Fig. A.6).

Rio Guayanés Saprolite - Mineralogy and Bulk Chemistry

The mud size fraction of the saprolite samples consist mainly of clay minerals followed by plagioclase (Table 2.A). No systematic trends in mineralogy are observed within the saprolite dataset.

Rio Guayanés Saprolite - Chemical Weathering Indexes

The Rio Guayanés saprolite samples have CIA values ranging from 69-97 which overlaps, but is higher than the fluvial sediments, overall (Fig. 7). The average CIA value for the

Rio Guayanés saprolite is 84, greater than any of the average values observed in the sediment samples (Fig. 8). As the surface area of the saprolite sediment increases a subsequent increase in the CIA value is also expected; this correlation is strongly observed within the saprolite samples (Fig. 13A, B). The Rio Guayanés saprolite sediment MFW plot (Fig. 9) also indicates the saprolite samples are significantly more weathered than the fluvial sediments as the saprolite samples trend most strongly towards the weathered vertex.

Rio Guayanés - Water Chemistry

The 2018 stream water samples had much higher concentrations of Na^+, Ca^{2+}, and Mg^{2+} and lower overall concentration in K^+ compared to the stream water in 2014 (Fig. 14). In 2018, the Na^+, Ca^{2+}, and Mg^{2+} concentrations generally decreased from proximal to distal until approximately 12 km where an increase and then subsequent decrease occurs (Fig. 14). Ca^{2+} and Mg^{2+} have very similar concentrations and follow similar trends to one another, while Na^+ concentration was consistently higher, but enriched relative to the solutes in 2018. K^+ concentrations increased from proximal to distal across the full distance sampled in 2018 (Fig. 14).

Tables and Figures:

Table 1. LANDSLIDE AREA AND VOLUME

Volume Equation:		$V = 0.0254 * A^{1.45}$*
Number of Landslides		116
Area (m^2)	Minimum	11
	Mean	238
	Maximum	2230
Volume (m^3)	Minimum	1
	Mean	110
	Maximum	1819

*Area and volume of all mapped landslides in Puerto Rico after Hurricane Maria (Regmi et al., 2014). The average volume of 110 m^3 indicates the average depth of the landslides is about 0.25 m and therefore very shallow. Full dataset in Appendix.

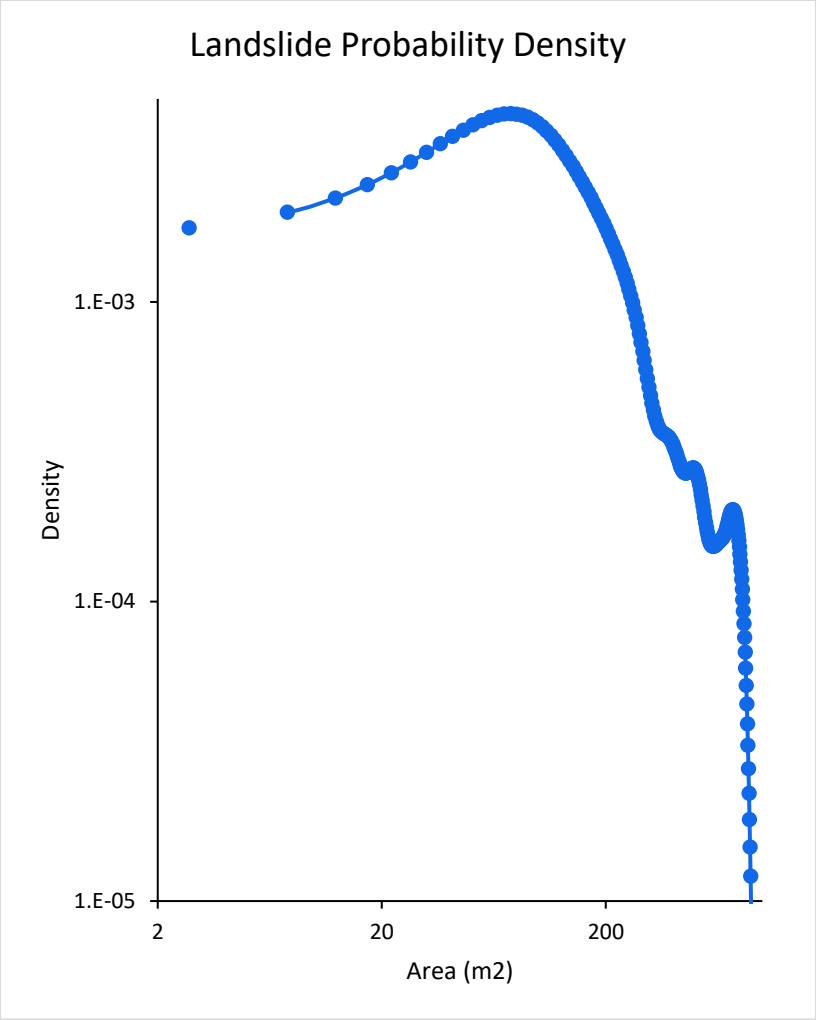

Figure 1: The probability density function of the one hundred sixteen mapped landslides in Puerto Rico illustrates that the majority of the landslides are relatively small, around 100 square meters.

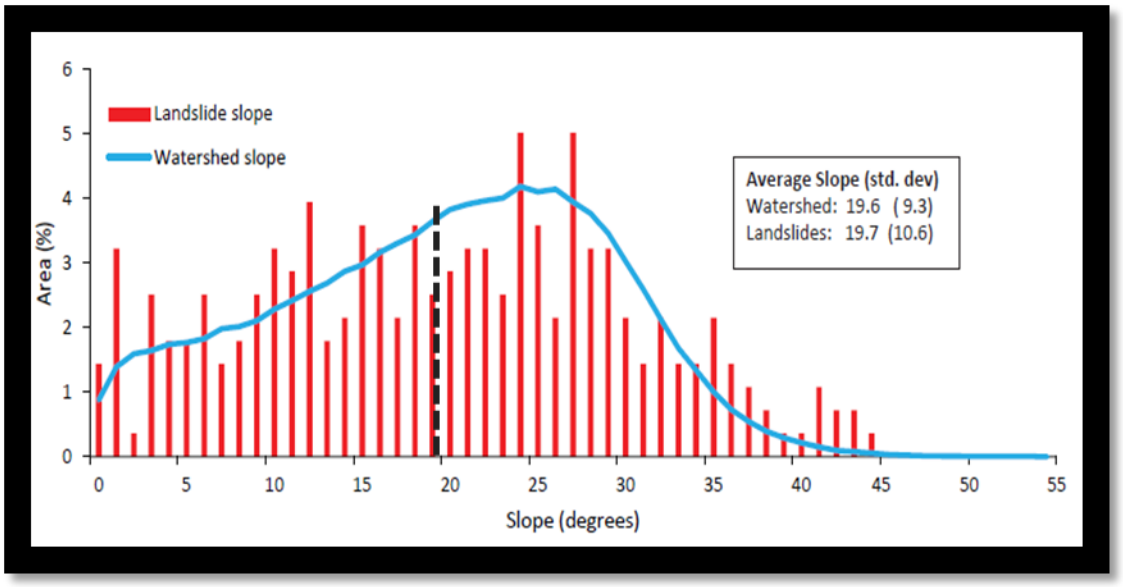

Figure 2: The right-skewed slope histogram illustrates that the majority of the slopes in the study region have a relatively gentle slope, around 24-26˚, versus being in areas of steeper slopes. The highest proportion of landslides correspond to the most prevalent slopes in the study region. The slope averages for the study area and the area of landslide occurrence are 19.6 and 19.7, respectively, (illustrated with the black dashed line) with very similar standard deviations. The occurrence of landslides at all slopes indicates one cannot predict landslide susceptibility based solely on slope of a region.

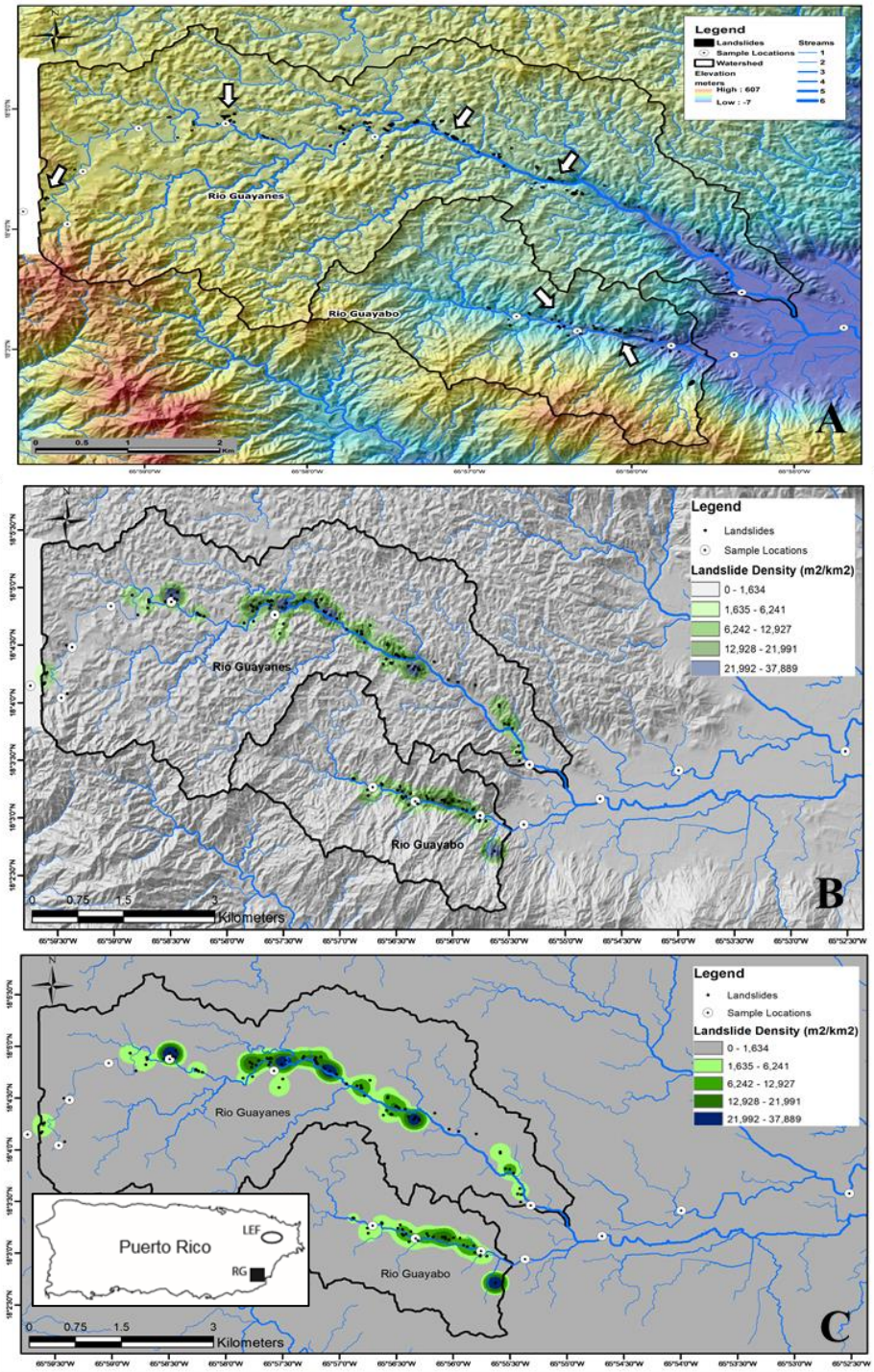

Figure 3: (A) Relief map of the Rio Guayanés located to the north and the Rio Guayabo in the south of the study region. Watersheds for the respective fluvial systems are outlined in black with sampling sites labeled as white circles and landslides indicated with black with arrows indicating landslides. (B & C) Inset map with study region highlighted by black box. Spatial density map for study region created using kernel density estimation of each of the mapped landslides within a 1 km^2 circular neighborhood.

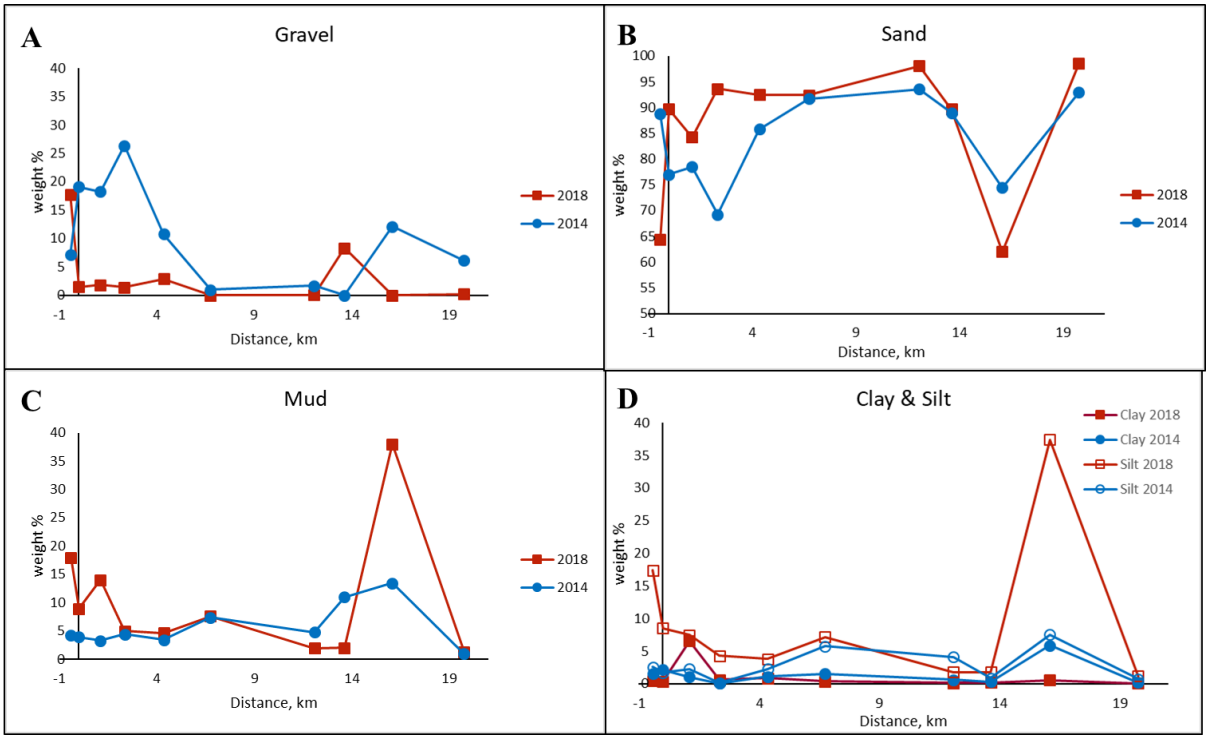

Figure 4: Weight percent of (A) gravel, (B) sand, (C) mud, (D) clay and silt in 2014 and 2018 as sampled downstream in the Rio Guayanés. The weight percent of gravel (A) 2018 versus 2014 is much lower, while the sand (B) and mud (C) size fractions are higher in 2018 than in 2014 in similar locations. The weight percent of clay (D) displays an opposite trend in 2014 versus 2018 with higher weight percent values in 2018 proximally versus distally while the silt displays very similar values between the two years.

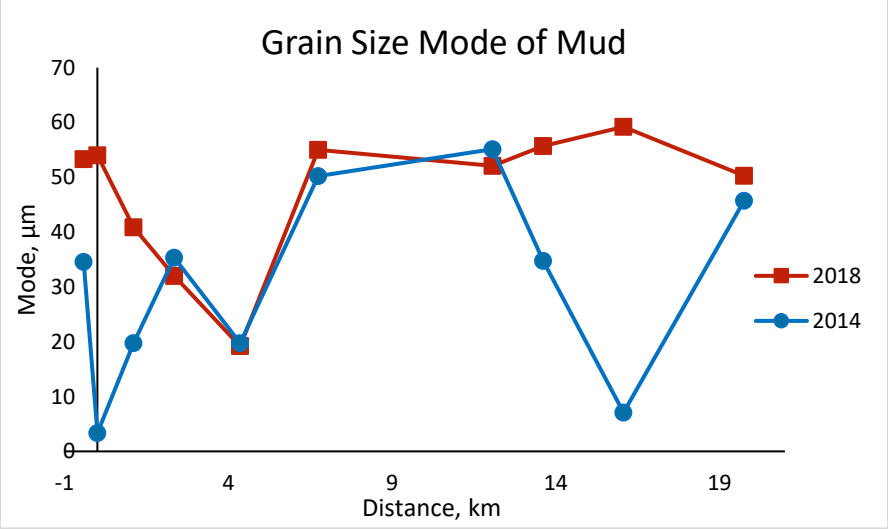

Figure 5: Mode grain size of Rio Guayanés mud samples taken in 2014 and 2018 versus distance. The 2018 mode displays a nearly opposite trend in the most proximal and distal samples compared to the 2014 samples, while the mid-stream portion trend similarly.

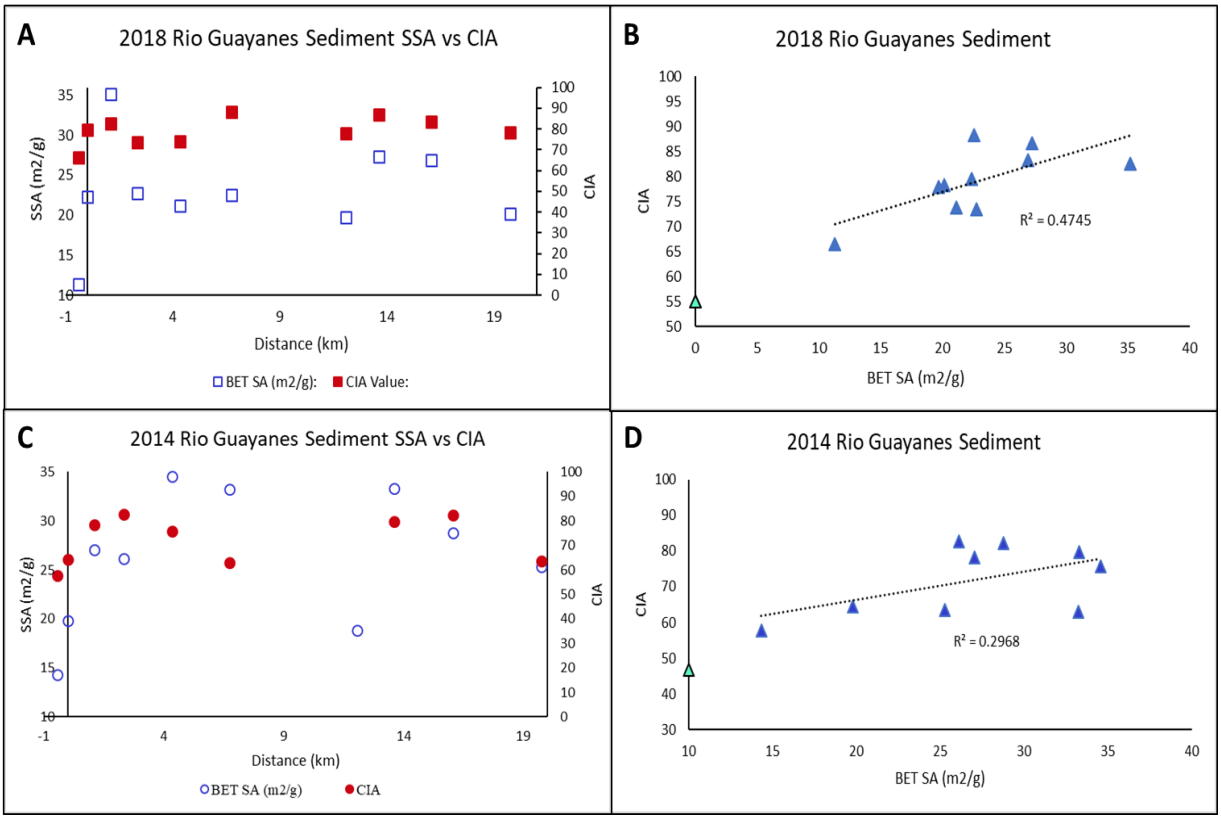

Figure 6: Rio Guayanés sediment and samples demonstrating a slight trend between the specific surface area and chemical index of alteration in 2018 (A & B). 2018 Rio Guayanés saprolite samples demonstrating a strong trend: as specific surface area increases an increase is also observed in the chemical index of alteration (C & D). The CIA value for sample 7 was not obtained by Joo et al. Teal triangle represents bedrock CIA in the study region.

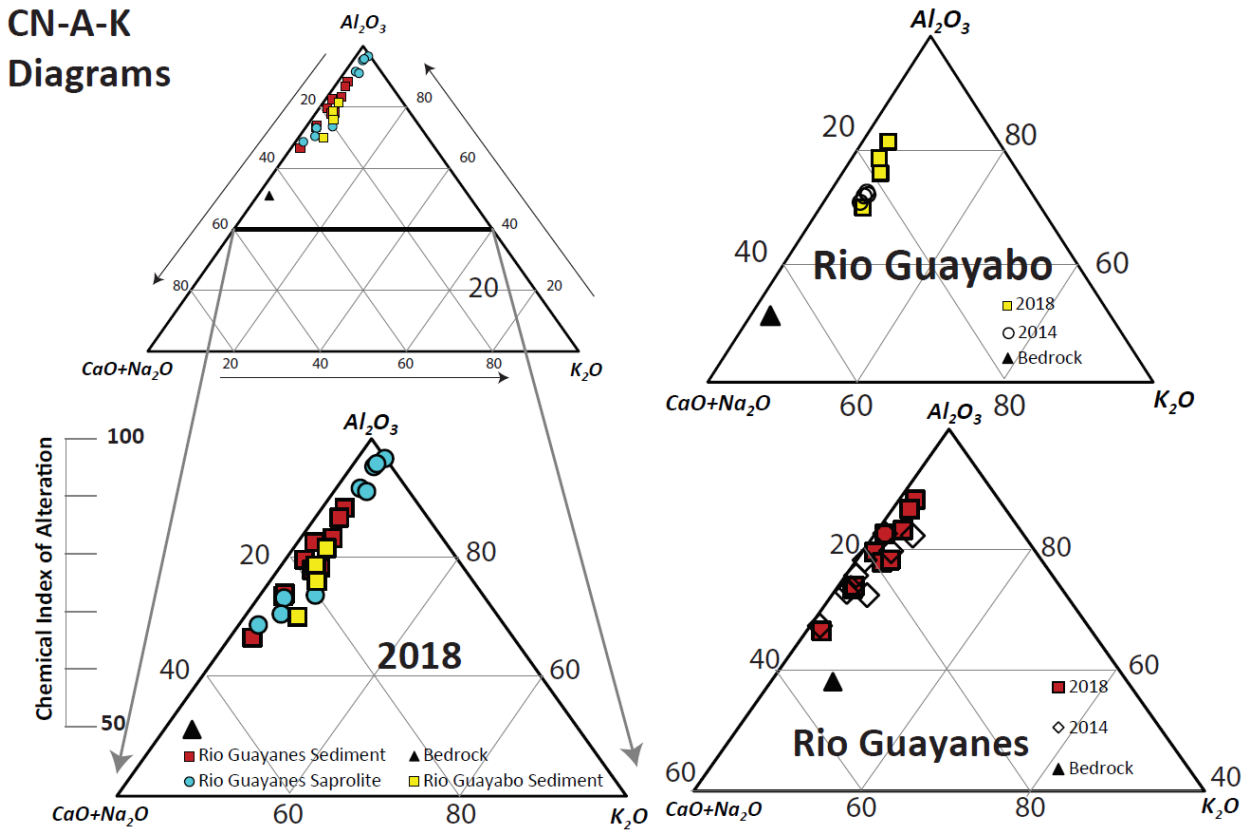

Figure 7: The chemical index of alteration for all samples. All of the samples collected in 2018 are shown on the left. Rio Guayanés sediment (red squares) and saprolite samples (blue circles), Rio Guayabo sediment (yellow squares), bedrock (black triangle).

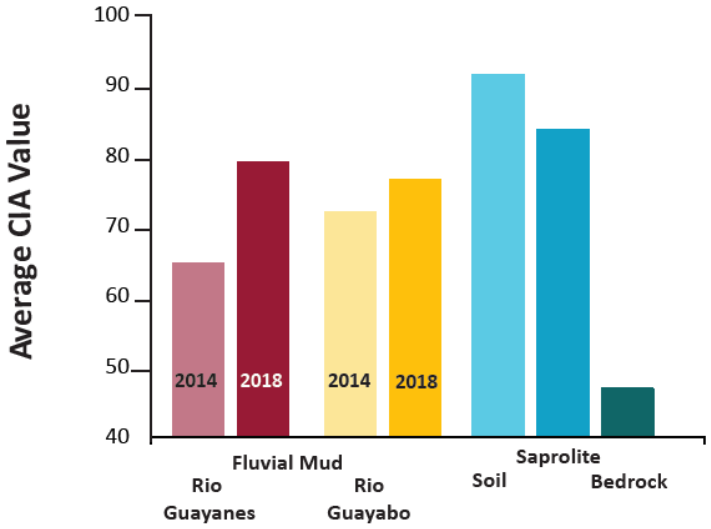

Figure 8: The average values of the chemical index of alteration for all sediment, soil, saprolite, and bedrock samples.

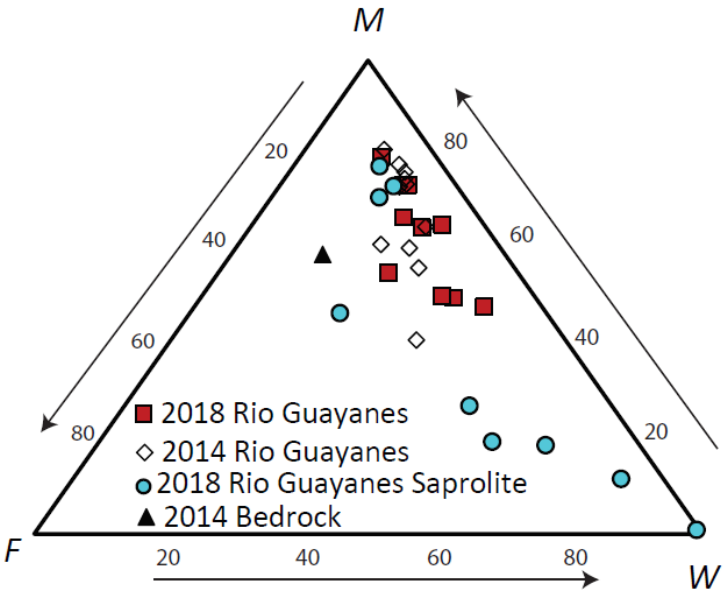

Figure 9: The MFW plot of Rio Guayanés sediment in 2018 (red squares) versus 2014 (open diamonds) and 2018 Rio Guayanés saprolite (blue circles). The 2018 sediment samples trend towards more weathered as well as the saprolite samples with some points trending towards the very weathered vertex (Ohta & Arai, 2007).

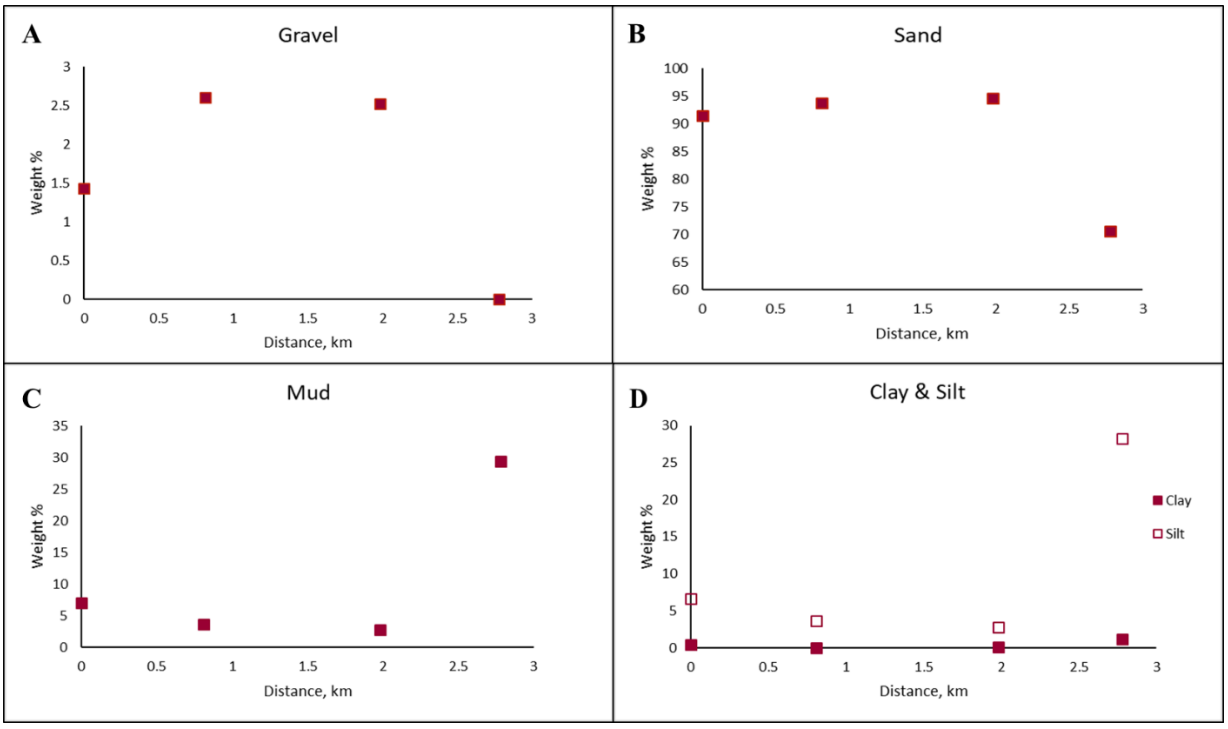

Figure 10: Rio Guayabo sediment weight percent plots versus distance for 2018. No systematic trends observed throughout the fluvial system.

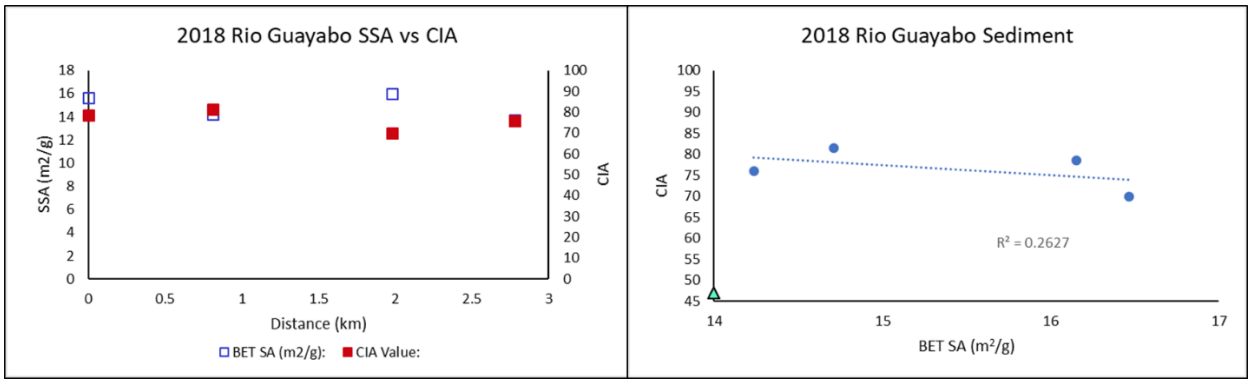

Figure 11: (A) Rio Guayabo sediment specific surface area and chemical index of alteration in 2018 versus distance, which shows strong correlation to one another. (B) 2018 Rio Guayabo specific surface area versus chemical index of alteration which shows no trend.

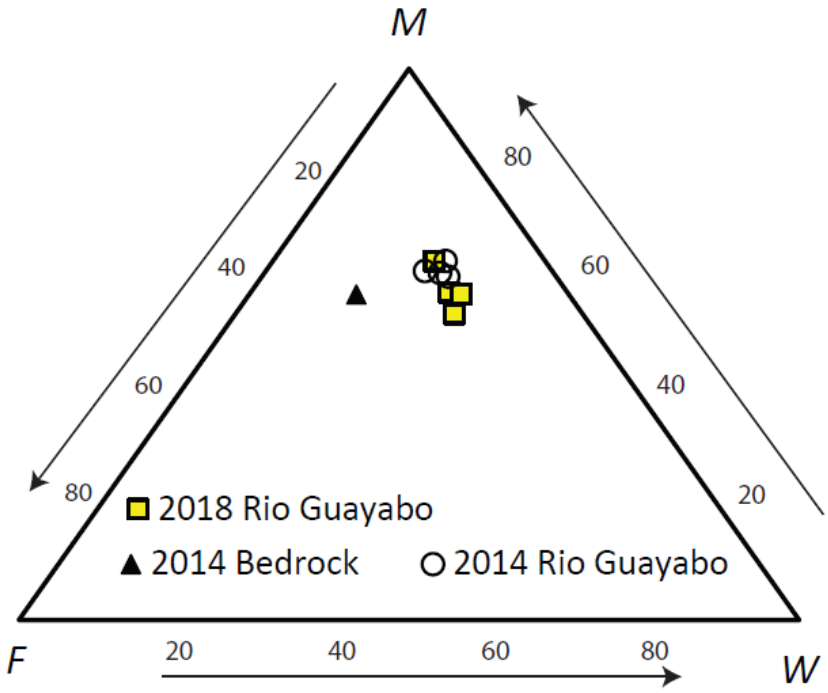

Figure 12: The MFW plot of 2018 Rio Guayabo samples shown in yellow squares, 2014 bedrock shown with black triangle, and 2014 Rio Guayabo samples shown in open circles. The 2018 Rio Guayabo samples trend towards more weathered compared to the 2014 samples (Ohta & Arai, 2007).

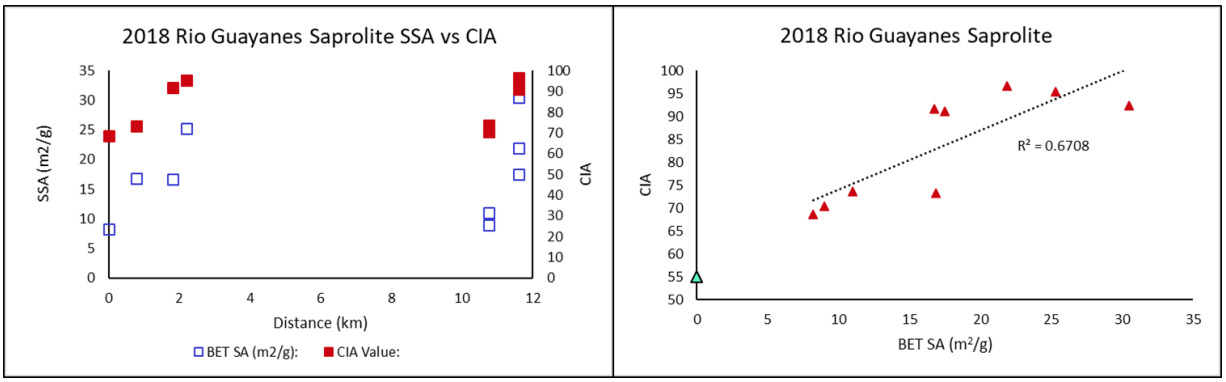

Figure 13: (A) Rio Guayanés saprolite sediment specific surface area and chemical index of alteration in 2018 versus distance, which shows a strong correlation to one another. (B) 2018 Rio Guayanés saprolite sediment specific surface area versus chemical index of alteration which shows a relatively strong trend.

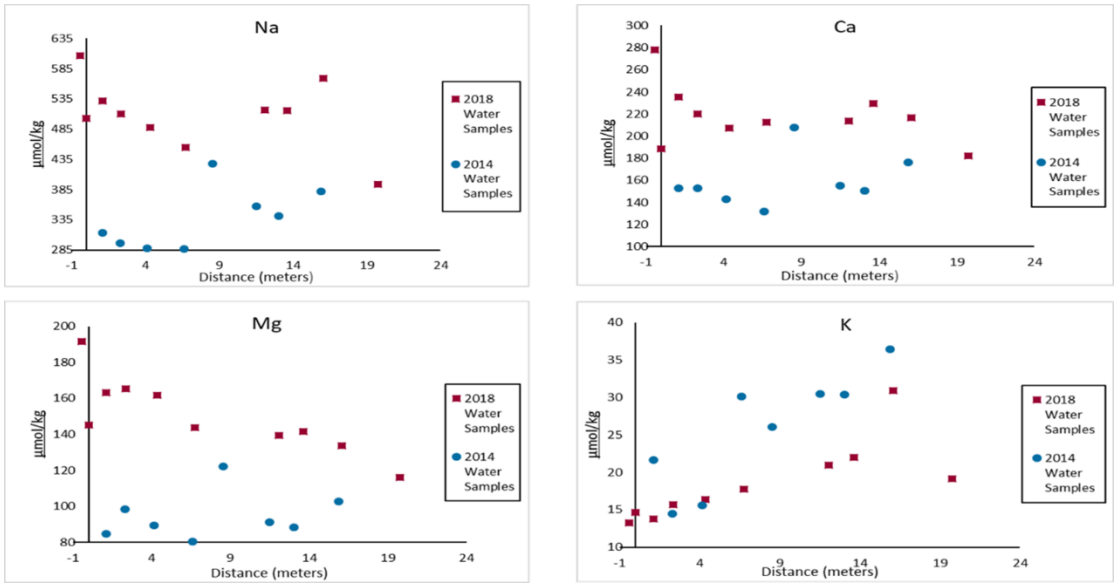

Figure 14: Cation concentrations in the Rio Guayanés stream water. Na^{+}, Ca^{2+}, and Mg^{2+} show a general decrease in concentration until approximately 12km and K^{+} shows a general increase distally in 2018. Mg^{2+} and Ca^{2+} show very similar trends to one another while Na^{+} is enriched compared to Mg^{2+} and Ca^{2+} but also shows a similar trend.

Discussion

As expected, a significant number of landslides occurred during the nine months following Hurricane Maria. The prevalence of landslides is likely due to anthropogenic forcings, such as deforestation, in addition to heavy amounts of precipitation which destabilized the slopes (Larsen & Parks, 1997; Murphy et al., 2012; Silva-Tulla et al., 2020). We initially hypothesized that landslides would sample the deeper bedrock (Joo et al., 2018). However, based on our results, we infer that the large amount of precipitation associated with Hurricane Maria (>500mm) led to the mass movement of the weathered topsoil and saprolite in relatively shallow landslides with average depths of only 0.25m (Table 1) along a range of slopes, with the majority occurring along $\leq 25^{\circ}$ slopes (Fig. 1, 2, and 3) (Bessette-Kirton et al., 2019; Iwahashi et al., 2012; Shiels & Walker, 2013; Silva-Tulla et al., 2020). The occurrence of landslides along a range of slopes (Fig. 2), but with the same lithology, indicates that neither one individually can predict landslide prevalence, but rather soil moisture variations play a significant role (Bessette-Kirton et al., 2019).

We hypothesized a decrease in the weathering index values of the mud size fraction in samples collected after Hurricane Maria, as Joo et al. (2018) hypothesized that the sediment delivered to the fluvial system via mass wasting would be derived from less-weathered bedrock. Instead, the increased CIA values of samples in 2018 relative to those collected in 2014 (Fig. 7, 8) likely reflects the introduction of more weathered soils rather than less weathered bedrock as the landslides in the region have a probability density function of relatively small, shallow landslides on $\leq 25^{\circ}$ slopes (Fig. 1, 2). However, landslides observed in areas of higher slopes may be sampling deeper, less weathered materials (Fig. 2). The MFW plot also indicates that the 2018 sediment is more weathered overall compared to the samples collected in 2014 (Fig. 9 and

13). This further supports the likelihood of more weathered sediment having been delivered to the fluvial system via shallow landslides instead of deep-seated landslides as a result of Hurricane Maria (Silva-Tulla et al., 2020).

We also expected the grain size within the mud component would increase post Hurricane Maria due to the delivery of less weathered sediments to the stream via landslides. The results indicate a left-skewed (coarser) distribution in all of the 2018 samples collected (Fig. A.1, 2, and 3) indicating more coarse-grained sediment overall. In the Rio Guayanés, a decrease in the amount of gravel delivered to the proximal portion of the stream is observed in 2018 versus in 2014, but the sand, mud, silt, and clay size fractions are coarser grained (Fig. 4). The medial portion of the stream also displays lower gravel content in 2018 versus 2014 while the sand is consistently higher which is interesting because of the amount of landslides present in this area is the greatest and we would expect for the gravel to be more abundant in 2018 comparably with the sand if the landslides were sampling deeper bedrock (Fig. 4). The weight percentage of the mud fraction is low in the medial portion of the stream and relatively comparable between the two years which correlates with more coarse grained material expected in the fluvial system (Fig. 4). The most distal samples, specifically sample 8, occurs just below the confluence of the Rio Guayanés and Rio Guayabo and exhibits the second highest weight percent of gravel with the sand beginning to decrease while the mud, silt, and clay are all comparable (Fig. 4). One would expect the smaller size material to settle out of the fluvial system distally of the area of highest relief (samples one through 6) which is exactly the weight percent trend of the mud, silt, and clay in 2018 (Fig. 4). As noted by Roda-Boluda et al. (2018), more coarse sediment is delivered to the fluvial system in areas prone to landslides which tend to

be areas affected by events such as hurricanes and/or anthropogenic forcings which leads to vegetation removal.

The particle size mode indicates there is a delivery of coarser grained mud size fraction sediments to the fluvial system upstream, a decrease mid-stream, followed by an increase downstream (Fig. 5) (Struck et al., 2015). This indicates that coarser sediment was delivered to the Rio Guayanés fluvial system in 2018. If the sediment was more weathered, and perhaps exhibited kaolinite, which would be a proxy for extensive weathering under humid climates, the mode distribution would illustrate a smaller grain size overall and more specifically distally as fines tend to be transported the farthest and deposition is more likely to occur distally (Table A.1). The particle mode from 2014 illustrates no trend with distance.

The mineralogy results from the x-ray diffraction data indicate no systematic trend from proximal to distal (Table A.1). An observed systematic trend downstream in both particle mode and mineralogy would indicate sorting within the fluvial system is occurring as well as a change in the sediment source, neither of which were observed. If landslides are the dominant source of sediment to the streams, we would not expect to see a trend in mineralogy as we moved downstream, but instead we would expect to see variability in mineralogy related to distance (Table A.1).

Results from the aqueous cation concentration in the stream were similar to the results obtained by Joo et al. (2018) in that the Na^+, Ca^{2+}, and Mg^{2+} generally decreased distally while the K^+ increased (Fig. 14) and the overall concentration of the solutes in 2018 was greater than in 2014 for every cation with the exception of K^+ (Fig. 14) (White et al., 1998). This prediction by Joo et al. (2108) of greater amounts of cations which could be interpreted as available for

eventual carbonate precipitation downstream following a mass wasting event, is supported by the 2018 data.

Pre-Hurricane Maria we observed anomalously low CIA values (Fig. 8 and 9) (Joo et al., 2018) in the fluvial sediment which could possibly be attributed to deeper seated landslides delivering partially weathered regolith to the fluvial systems. These deeper seated landslides could be a result of tectonics (Bessette-Kirton et al., 2019; Masson & Scanlo, 1991; Reid & Taber, 1918) and/or anthropogenic forcing such as the construction of roads in the hillsides (Larsen & Parks, 1997; Murphy et al., 2012). Therefore, the transport mechanism is essentially the same, just a variation in the initial cause of the mass wasting and the weathering indices are not indicative of the rate of climate change.

While the initial disturbance of mass wasting events can seem detrimental as a carbon source through the destruction of vegetation, the reactions immediately following have some interesting implications (Fisk et al., 2013; Hall et al., 2020). The exposure of fresh bedrock through mechanical weathering from landslides propagates chemical weathering as water is enabled to interact with bedrock (Oliva et al., 2003). Fresh surfaces lack weathered rindlets (Turner et al., 2003), soils, or clay which leads to an increase in the specific surface area and makes them more prone to chemical weathering (White et al., 1998). The sediment associated with landslides can be deposited a few ways, such as directly to a fluvial system or stored on hillslopes (Clark et al., 2016; Hilton et al., 2011). With the occurrence of shallow landslides not necessarily reaching the fluvial system, this implies deposition of the material on hillslopes which can result in longer-term carbon sequestration due to chemical weathering (Clark et al., 2016; Fisk et al., 2013; Hall et al., 2020; Hilton et al., 2011; Ramos-Scharrón & Arima, 2019). Sediment entering fluvial systems tend to have a more variable and unconstrained outcome in

regards to carbon sequestration (Clark et al., 2016; Ramos-Scharrón & Arima, 2019) but deposition in basins results in a long-term net carbon sink. The landslide scarps are perhaps a major factor in regional carbon sequestration through the recovery of the forest acting as carbon sinks (Fisk et al., 2013; Hall et al., 2020; Hilton et al., 2011) as opposed to mature forests which do not sequester as much atmospheric CO_2 (Hilton et al., 2011). The magnitude of a storm and associated rainfall accumulation amounts coupled with a variety of variables such as lithology, anthropogenic disturbances, and degree of hillslope are significant on the effect of carbon sequestration.

Conclusions and Implications

The sediment deposited in the basin downstream will display a signal of more highly weathered material delivered to the fluvial system from the shallow landslides associated with events of high precipitation such as Hurricane Maria. Deep seated landslides are driven by tectonics or road building and sample the regolith and therefore display lower CIA reflective of less chemical weathering. The difference observed in the CIA values within four years is not reflective of the degree of climate change, but rather a large number of small landslide events are key to the release of large volumes of pre-weathered material. This subtle change in the transport mechanism can result in rather large differences in the weathering values recorded by the fluvial system.

These same implications can be translated to interpreting chemical weathering indexes on Mars particularly when analyzing fluvial sediments within impact craters. Impact craters have a significant portion of sediment delivered to the floor via mass wasting along the crater walls. Tectonics on Mars result in large landslides, while a rainy period would result in shallow

landslides. This study indicates that subtle changes in the size of the landslides providing sediment from the crater walls can derive very different CIA values.

Appendix

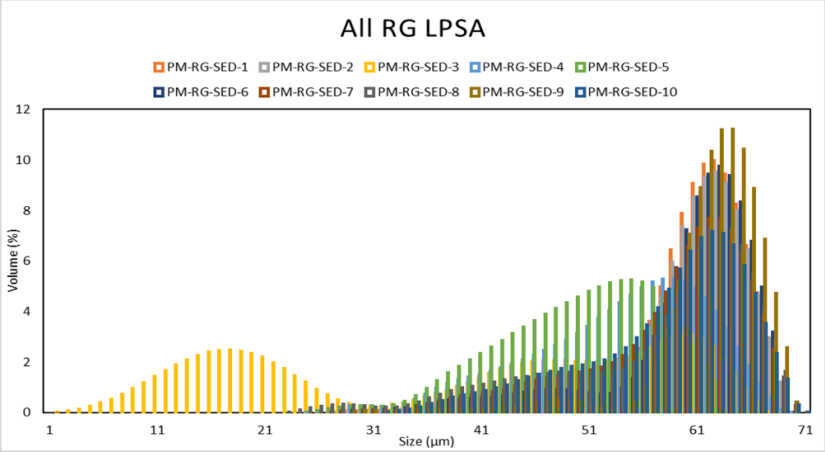

Figure A.1: Laser particle size analysis of all 2018 Rio Guayanés sediment samples. All, with the exception of PM-RG-SED-3, illustrating a left skewed histogram showing that the mud size fraction consists of more coarse-grained sediment overall. PM-RG-SED-3 illustrates a strongly bimodal distribution.

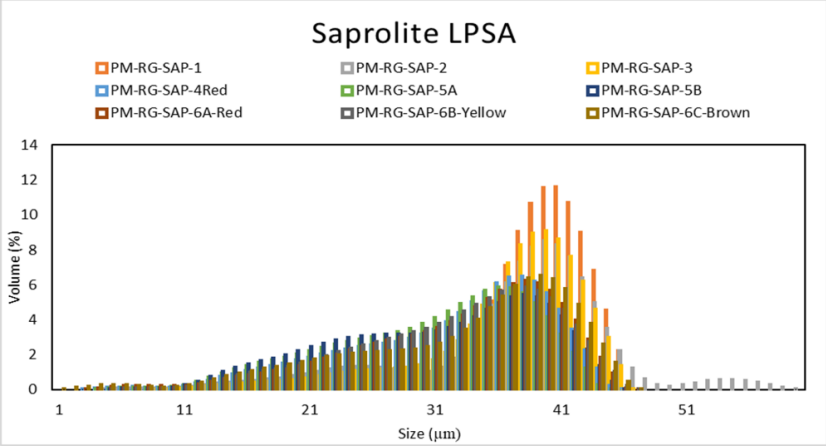

Figure A.2: Laser particle size analysis of all 2018 Rio Guayanés saprolite samples. All samples display a left skewed distribution of coarse-grained sediment.

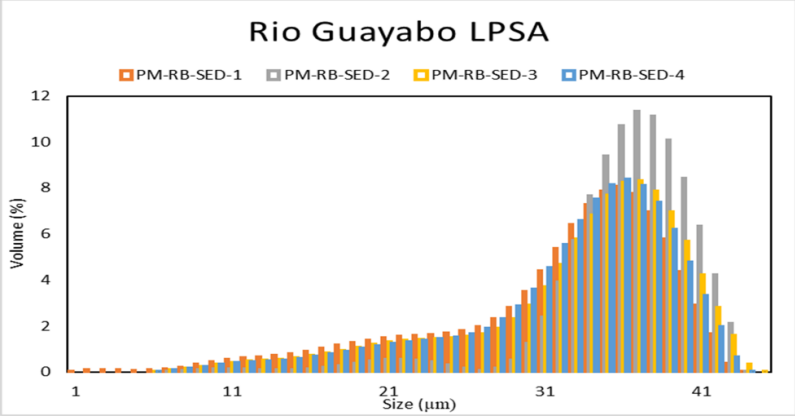

Figure A.3: Laser particle size analysis of all the 2018 Rio Guayabo samples. SED-1 has the smallest grain size present, all have a left skewed distribution with SED-2 having the most coarse-grained materials.

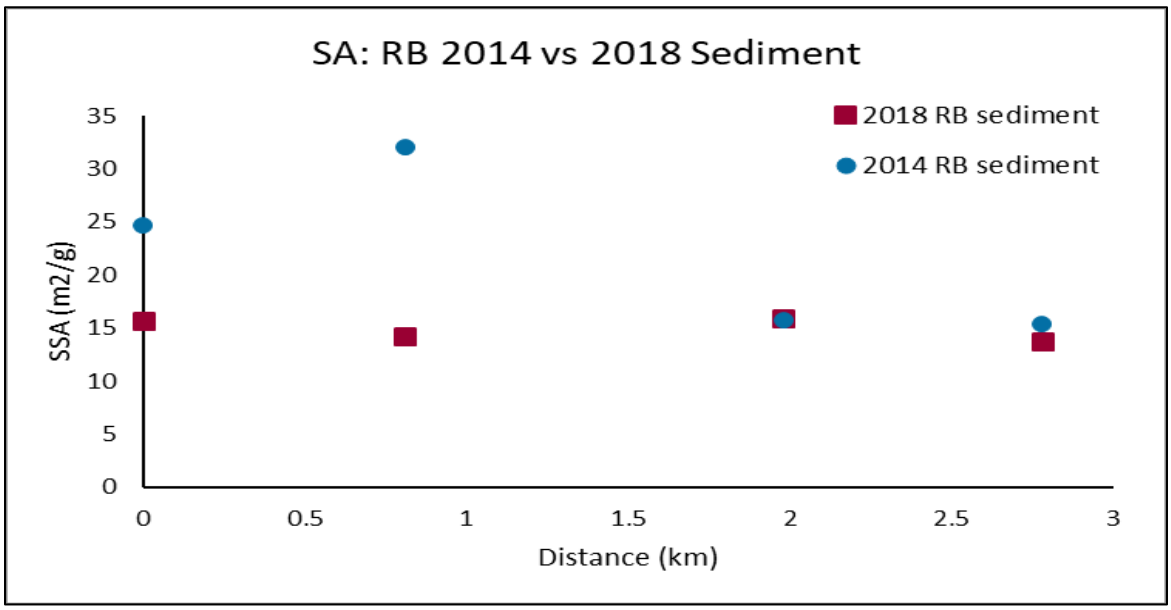

Figure A.4: Rio Guayabo sediment surface area versus distance for 2014 and 2018. The surface area in 2018 remains rather constant and 2014 illustrates only slight variability.

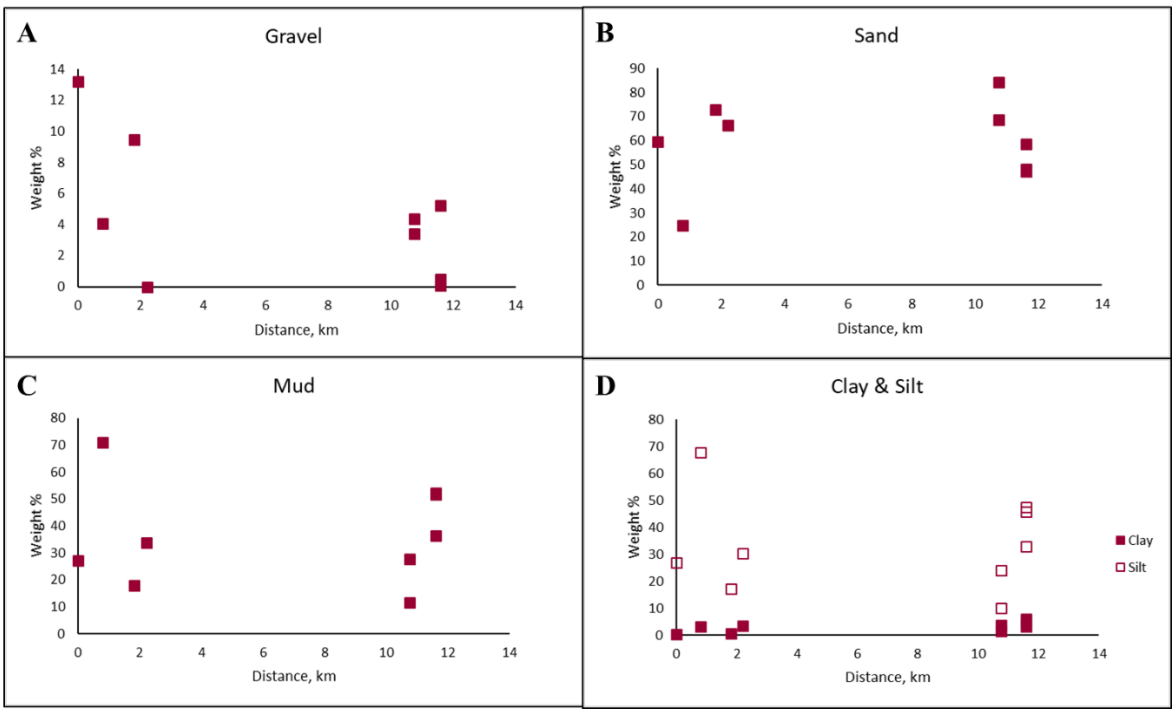

Figure A.5: Rio Guayanés saprolite weight percent versus distance for all size fractions.

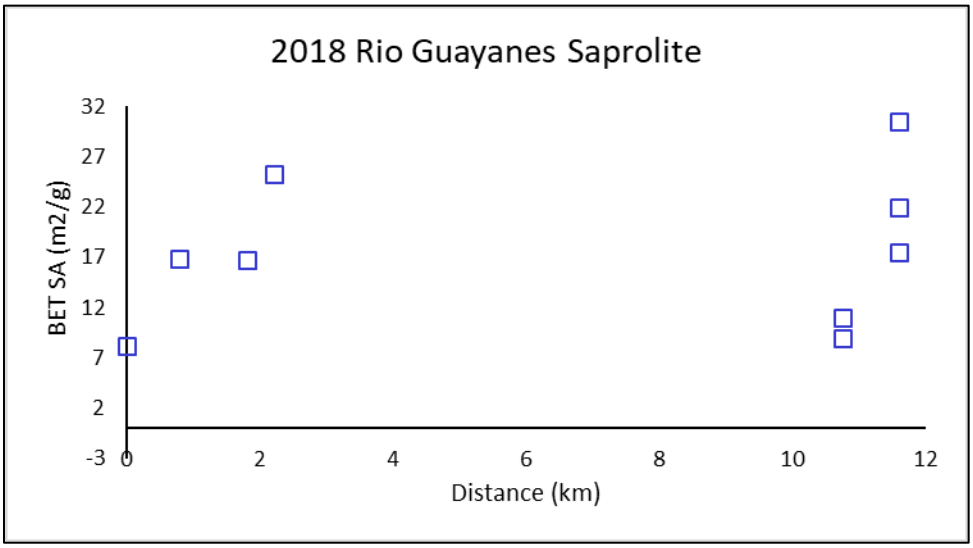

Figure A.6: The 2018 Rio Guayanés saprolite mud size fraction specific surface area increases and then decreases downstream. The last sample, 6A, B, C illustrates strong variability in surface area within the same outcrop. There were no saprolite samples collected in 2014 for comparison.

Table A.1: Mineralogy relative percentages from x-ray diffraction for all 2018 saprolite and sediments and comparable collection locations from 2014 sediments for both the Rio Guayanés and Rio Guayabo.

Sample Name	Distance (km)	Quartz	Plagioclase	Amphibole	Micas	Clays
2018 Rio Guayanés Samples						
PM-RG-SED-1	-0.418	11	55.6	21.1	0	12.3
PM-RG-SED-2	0	17.2	45.4	14.9	1.9	20.6
PM-RG-SED-3	1.103	21.2	24.1	19.8	0	34.9
PM-RG-SED-4	2.345	18.1	52.1	21.2	0	8.5
PM-RG-SED-5	4.357	16.8	35.2	21.7	0	26.3
PM-RG-SED-6	6.744	11.5	28.3	8.8	0	51.2
PM-RG-SED-7	12.074	14.5	51.1	8.4	0.0	26.0
PM-RG-SED-8	13.622	14.1	34.9	9.3	0	41.8
PM-RG-SED-10	16.073	11.4	40.4	7.5	0	40.8
PM-RG-SED-9	19.755	10.5	50.1	14.4	0	25.1
2018 Rio Guayanés Saprolite Samples						
PM-RG-SAP-1	0	9.2	72.2	11.0	2.2	5.4
PM-RG-SAP-2	0.79	0	40.9	28.5	9.1	21.5
PM-RG-SAP-3	1.81	2.7	22.9	3.3	3.2	67.9
PM-RG-SAP-4Red	2.21	0.1	1.3	10.7	6.6	81.3
PM-RG-SAP-5A	10.76	3.1	29.9	14.7	31.2	21.0
PM-RG-SAP-5B	10.76	9.7	25.1	0.0	26.0	38.0
PM-RG-SAP-6A	11.60	2.1	3.5	0.0	1.4	93.0
PM-RG-SAP-6B	11.60	0.8	17.8	9.5	0.0	72.0
PM-RG-SAP-6C	11.60	0.7	19.9	7.1	2.9	69.3
2018 Rio Guayabo Samples						
PM-RB-SED-1	0	0	23	21.9	23.3	31.8
PM-RB-SED-2	0.81	0	44.4	13.7	0	42
PM-RB-SED-3	1.98	0	41.9	15.3	8.9	34
PM-RB-SED-4	2.78	0	37.7	12.8	22.2	27.3
2014 Samples						
RG-14-1 (RGTr-b)	-2	8.9	42.5	16.5	9.6	21.7
RG-14-3 (a)	0	8.2	33.4	13.8	10.7	33.9
RG-14-4 (b)	1.1	1.1	2.4	93.0	0	3.5
RG-14-11 (c)	2.31	4.4	26.2	38.8	0	30.6
RG-14-13 (e)	4.15	7.6	40.2	25.6	0	26.6
RG-14-5 (f)	6.61	8.2	28.3	18.5	11.3	33.7
RG-14-6 (i)	11.72	nd	nd	nd	nd	nd
RG-14-9 (k)	13.06	3.6	19.7	9.3	22.8	44.6
RG-14-10 (l)	15.89	11.1	38.6	14.6	8.6	27.2
RG-14-14 (m)	19.56	6.7	31.7	5.5	16.4	39.7

Table A.2: Full dataset of all mapped landslides with calculated volume from Regmi et al. (2014) and depth.

Landslide number	Area (m^2)	Volume (m^3)	Depth (m)	Min of Depth	Max of Depth	Average Depth (m)
1	124.69	27.78	0.22	0.07	0.82	0.25
2	110.24	23.24	0.21			
3	282.79	91.09	0.32			
4	43.63	6.06	0.14			
5	165.80	42.00	0.25			
6	81.90	15.10	0.18			
7	2229.69	1818.81	0.82			
8	60.17	9.66	0.16			
9	163.50	41.16	0.25			
10	198.79	54.64	0.27			
11	133.98	30.83	0.23			
12	484.49	198.84	0.41			
13	180.14	47.37	0.26			
14	111.26	23.55	0.21			
15	80.86	14.83	0.18			
16	110.24	23.24	0.21			
17	70.46	12.14	0.17			
18	566.04	249.15	0.44			
19	43.70	6.07	0.14			
20	30.23	3.56	0.12			
21	80.55	14.74	0.18			
22	125.38	28.01	0.22			
23	91.98	17.87	0.19			
24	118.62	25.84	0.22			
25	223.83	64.90	0.29			
26	82.85	15.36	0.19			
27	43.83	6.10	0.14			
28	58.43	9.26	0.16			
29	79.66	14.51	0.18			
30	10.99	0.82	0.07			
31	257.33	79.44	0.31			
32	78.26	14.14	0.18			
33	11.59	0.89	0.08			
34	175.52	45.61	0.26			
35	736.93	365.26	0.50			
36	424.97	164.42	0.39			

37	19.20	1.84	0.10
38	53.07	8.05	0.15
39	92.45	18.01	0.19
40	174.25	45.14	0.26
41	500.37	208.36	0.42
42	38.35	5.03	0.13
43	195.12	53.18	0.27
44	143.54	34.08	0.24
45	49.74	7.33	0.15
46	39.99	5.34	0.13
47	46.07	6.56	0.14
48	122.79	27.17	0.22
49	72.40	12.63	0.17
50	79.01	14.34	0.18
51	1643.80	1169.00	0.71
52	65.85	11.01	0.17
53	401.99	151.68	0.38
54	284.13	91.71	0.32
55	155.27	38.19	0.25
56	80.06	14.61	0.18
57	53.46	8.14	0.15
58	84.34	15.76	0.19
59	381.52	140.62	0.37
60	97.12	19.34	0.20
61	269.16	84.79	0.32
62	167.76	42.72	0.25
63	126.38	28.33	0.22
64	170.48	43.73	0.26
65	170.54	43.75	0.26
66	245.59	74.24	0.30
67	61.16	9.89	0.16
68	209.47	58.95	0.28
69	1751.94	1282.15	0.73
70	142.08	33.57	0.24
71	226.10	65.85	0.29
72	136.73	31.76	0.23
73	30.22	3.56	0.12
74	90.51	17.46	0.19
75	194.39	52.89	0.27
76	505.00	211.16	0.42
77	69.44	11.89	0.17
78	123.28	27.33	0.22
79	671.99	319.53	0.48

80	1369.70	897.31	0.66
81	805.26	415.37	0.52
82	62.62	10.23	0.16
83	67.41	11.39	0.17
84	101.65	20.66	0.20
85	289.76	94.36	0.33
86	350.59	124.39	0.35
87	205.01	57.14	0.28
88	45.29	6.40	0.14
89	41.62	5.66	0.14
90	39.61	5.27	0.13
91	624.56	287.35	0.46
92	742.64	369.37	0.50
93	60.02	9.62	0.16
94	61.84	10.05	0.16
95	83.65	15.57	0.19
96	154.30	37.84	0.25
97	26.93	3.01	0.11
98	38.97	5.14	0.13
99	72.36	12.62	0.17
100	144.53	34.42	0.24
101	214.71	61.10	0.28
102	2003.33	1557.31	0.78
103	259.52	80.43	0.31
104	248.00	75.30	0.30
105	17.71	1.64	0.09
106	99.77	20.11	0.20
107	110.66	23.37	0.21
108	76.62	13.71	0.18
109	364.04	131.37	0.36
110	71.13	12.31	0.17
111	59.90	9.60	0.16
112	147.61	35.48	0.24
113	228.19	66.74	0.29
114	59.66	9.54	0.16
115	80.19	14.65	0.18
116	54.86	8.45	0.15

Aristizábal, E., Roser, B., & Yokota, S. (2005). Tropical chemical weathering of hillslope deposits and bedrock source in the Aburrá Valley, northern Colombian Andes. *Engineering Geology*. https://doi.org/10.1016/j.enggeo.2005.08.001

Attal, M., Mudd, S. M., Hurst, M. D., Weinman, B., Yoo, K., & Naylor, M. (2015). Impact of change in erosion rate and landscape steepness on hillslope and fluvial sediments grain size in the Feather River basin (Sierra Nevada, California). *Earth Surface Dynamics*, *3*(1), 201–222. https://doi.org/10.5194/esurf-3-201-2015

Bessette-Kirton, E. K., Cerovski-Darriau, C., Schulz, W. H., Coe, J. A., Kean, J. W., Godt, J. W., Thomas, M. A., & Stephen Hughes, K. (2019). Landslides triggered by Hurricane Maria: Assessment of an extreme event in Puerto Rico. *GSA Today*, *29*(6). https://doi.org/10.1130/GSATG383A.1

Birdsey, R. A., & Weaver, P. L. (1982). The forest resources of Puerto Rico. *Resource Bulletin SO 85*, *85*, ii, 59 p. http://purl.access.gpo.gov/GPO/LPS83699

Bluth, G. J. S., & Kump, L. R. (1994). Lithologic and climatologic controls of river chemistry. *Geochimica et Cosmochimica Acta*, *58*(10), 2341–2359. https://doi.org/10.1016/0016-7037(94)90015-9

Brunauer, S., Emmett, P. H., & Teller, E. (1938). *Adsorption of Gases in Multimolecular Layers*. https://pubs.acs.org/sharingguidelines

Buss, H. L., Chapela Lara, M., Moore, O. W., Kurtz, A. C., Schulz, M. S., & White, A. F. (2017). Lithological influences on contemporary and long-term regolith weathering at the Luquillo Critical Zone Observatory. *Geochimica et Cosmochimica Acta*, *196*, 224–251. https://doi.org/10.1016/j.gca.2016.09.038

Caine, N. (1980). The Rainfall Intensity : Duration Control of Shallow Landslides and Debris Flows Author (s): Nel Caine Published by : Taylor & Francis , Ltd . on behalf of the Swedish Society for Anthropology and Geography Stable URL : https://www.jstor.org/stable/5204. *Geografiska Annaler: Series A, Physical Geography*, *62*(1–2), 23–27.

Clark, K. E., West, A. J., Hilton, R. G., Asner, G. P., Quesada, C. A., Silman, M. R., Saatchi, S. S., Farfan-Rios, W., Martin, R. E., Horwath, A. B., Halladay, K., New, M., & Malhi, Y. (2016). Storm-triggered landslides in the Peruvian Andes and implications for topography, carbon cycles, and biodiversity. *Earth Surface Dynamics*, *4*(1), 47–70. https://doi.org/10.5194/esurf-4-47-2016

Crozier, M. J. (2010). Deciphering the effect of climate change on landslide activity: A review. In *Geomorphology* (Vol. 124, Issues 3–4, pp. 260–267). https://doi.org/10.1016/j.geomorph.2010.04.009

Dou, J., Chang, K., Chen, S., Yunus, A. P., Liu, J., Xia, H., Zhu, Z., Informatics, E., District, H., & Thenkabail, P. S. (2015). *remote sensing*. *1*, 4318–4342. https://doi.org/10.3390/rs70404318

Emberson, R., Galy, A., & Hovius, N. (2018). Weathering of Reactive Mineral Phases in Landslides Acts as a Source of Carbon Dioxide in Mountain Belts. *Journal of Geophysical*

Research: Earth Surface, *123*(10), 2695–2713. https://doi.org/10.1029/2018JF004672

Fernandes, A. M., Conceição, F. T. da, Spatti Junior, E. P., Sardinha, D. de S., & Mortatti, J. (2016). Chemical weathering rates and atmospheric/soil CO2 consumption of igneous and metamorphic rocks under tropical climate in southeastern Brazil. *Chemical Geology*, *443*, 54–66. https://doi.org/10.1016/j.chemgeo.2016.09.008

Fisk, J. P., Hurtt, G. C., Chambers, J. Q., Zeng, H., Dolan, K. A., & Negrón-Juárez, R. I. (2013). The impacts of tropical cyclones on the net carbon balance of eastern US forests (1851-2000). *Environmental Research Letters*, *8*(4). https://doi.org/10.1088/1748-9326/8/4/045017

Fletcher, R. C., Buss, H. L., & Brantley, S. L. (2006). A spheroidal weathering model coupling porewater chemistry to soil thicknesses during steady-state denudation. *Earth and Planetary Science Letters*. https://doi.org/10.1016/j.epsl.2006.01.055

Gaillardet, J., Dupré, B., Louvat, P., & Allègre, C. J. (1999). Global silicate weathering and CO2 consumption rates deduced from the chemistry of large rivers. *Chemical Geology*. https://doi.org/10.1016/S0009-2541(99)00031-5

Gariano, S. L., & Guzzetti, F. (2016). Landslides in a changing climate. *Earth-Science Reviews*, *162*, 227–252. https://doi.org/10.1016/j.earscirev.2016.08.011

Goldberg, K., & Humayun, M. (2010). *The applicability of the Chemical Index of Alteration as a paleoclimatic indicator : An example from the Permian of the Paraná Basin , Brazil*. *293*, 175–183. https://doi.org/10.1016/j.palaeo.2010.05.015

Guzzetti, F., Ardizzone, F., Cardinali, M., Galli, M., Reichenbach, P., & Rossi, M. (2008). Distribution of landslides in the Upper Tiber River basin, central Italy. *Geomorphology*, *96*(1–2), 105–122. https://doi.org/10.1016/j.geomorph.2007.07.015

Hall, J., Muscarella, R., Quebbeman, A., Arellano, G., Thompson, J., Zimmerman, J. K., & Uriarte, M. (2020). Hurricane-Induced Rainfall is a Stronger Predictor of Tropical Forest Damage in Puerto Rico Than Maximum Wind Speeds. *Scientific Reports*, *10*(1), 1–10. https://doi.org/10.1038/s41598-020-61164-2

Harris, W., & White, G. N. (2008). *X-Ray Diffraction Techniques for Soil Mineral Identification*.

Hilton, R. G., Meunier, P., Hovius, N., Bellingham, P. J., & Galy, A. (2011). Landslide impact on organic carbon cycling in a temperate montane forest. *Earth Surface Processes and Landforms*, *36*(12), 1670–1679. https://doi.org/10.1002/esp.2191

Hubert, J. F., & Filipov, A. J. (1989). Debris-flow deposits in alluvial fans on the west flank of the White Mountains, Owens Valley, California, U.S.A. *Sedimentary Geology*, *61*(3–4), 177–205. https://doi.org/10.1016/0037-0738(89)90057-2

Iwahashi, J., Kamiya, I., & Yamagishi, H. (2012). Geomorphology High-resolution DEMs in the study of rainfall- and earthquake-induced landslides : Use of a variable window size method in digital terrain analysis. *Geomorphology*, *153–154*, 29–38. https://doi.org/10.1016/j.geomorph.2012.02.002

Joo, Y. J., Madden, M. E. E., & Soreghan, G. S. (2018). Anomalously low chemical weathering

in fluvial sediment of a tropical watershed (Puerto Rico). *Geology*, *46*(8), 691–694. https://doi.org/10.1130/G40315.1

Keellings, D., & Hernández Ayala, J. J. (2019). Extreme Rainfall Associated With Hurricane Maria Over Puerto Rico and Its Connections to Climate Variability and Change. *Geophysical Research Letters*, *46*(5), 2964–2973. https://doi.org/10.1029/2019GL082077

Larsen, M. C. (2000). Analysis of 20th century rainfall and streamflow to characterize drought and water resources in puerto rico. *Physical Geography*, *21*(6), 494–521. https://doi.org/10.1080/02723646.2000.10642723

Larsen, M. C., & Parks, J. E. (1997). How wide is a road? The association of roads and mass-wasting in a forested montane environment. *Earth Surface Processes and Landforms*, *22*(9), 835–848. https://doi.org/10.1002/(SICI)1096-9837(199709)22:9<835::AID-ESP782>3.0.CO;2-C

Larsen, M. C., & Torres-Sánchez, A. J. (1998). The frequency and distribution of recent landslides in three montane tropical regions of Puerto Rico. *Geomorphology*. https://doi.org/10.1016/S0169-555X(98)00023-3

Lehmann, P., Gambazzi, F., Suski, B., Baron, L., Askarinejad, A., Sarah, M., Holliger, K., & Or, D. (2013). *Evolution of soil wetting patterns preceding a hydrologically induced landslide inferred from electrical resistivity survey and point measurements of volumetric water content and pore water pressure*. *49*, 7992–8004. https://doi.org/10.1002/2013WR014560

Lepore, C., Kamal, S. A., Shanahan, P., & Bras, R. L. (2012). Rainfall-induced landslide susceptibility zonation of Puerto Rico. *Environmental Earth Sciences*, *66*(6), 1667–1681. https://doi.org/10.1007/s12665-011-0976-1

Liu, T. K., Odell, R. T., Etter, W. C., & Thornburn, T. H. (1966). A comparison of clay contents determined by hydrometer and pipette methods using reduced major axis analysis. *Proceedings /*, *30*(6), 665.

Malvern. (1997). *Manual: Mastersizer S & X Getting Started Issue 1.3*.

Martinuzzi, S., Gould, W. A., & Ramos González, O. M. (2007). Land development, land use, and urban sprawl in Puerto Rico integrating remote sensing and population census data. *Landscape and Urban Planning*. https://doi.org/10.1016/j.landurbplan.2006.02.014

Masson, D. G., & Scanlo, K. M. (1991). *The neotectonic setting of Puerto Rico*. https://pubs.geoscienceworld.org/gsa/gsabulletin/article-pdf/103/1/144/3380967/i0016-7606-103-1-144.pdf

Miller, D. J., & Burnett, K. M. (2007). *Effects of forest cover , topography , and sampling extent on the measured density of shallow , translational landslides*. *43*(November 2006), 1–23. https://doi.org/10.1029/2005WR004807

Monroe, W. H. (1980). *Geology of the Middle Tertiary Forrnations of Puerto Rico Geological Survey Professional Paper 953*.

Moore, O. W., Buss, H. L., & Dosseto, A. (2019). Incipient chemical weathering at bedrock fracture interfaces in a tropical critical zone system, Puerto Rico. *Geochimica et*

Cosmochimica Acta, *252*, 61–87. https://doi.org/10.1016/j.gca.2019.02.028

Murphy, S. F., Stallard, R. F., Larsen, M. C., & Gould, W. A. (2012). Physiography, geology, and land cover of four watersheds in eastern Puerto Rico. *Water Quality and Landscape Processes of Four Watersheds in Eastern Puerto Rico*, 1–24.

Nesbitt, H. W., & Young, G. M. (1982). Early Proterozoic climates and plate motions inferred from major element chemistry of Intites. In *Nature* (Vol. 299).

Ohta, T., & Arai, H. (2007). Statistical empirical index of chemical weathering in igneous rocks: A new tool for evaluating the degree of weathering. *Chemical Geology*. https://doi.org/10.1016/j.chemgeo.2007.02.017

Oliva, P., Viers, J., & Dupré, B. (2003). Chemical weathering in granitic environments. *Chemical Geology*. https://doi.org/10.1016/j.chemgeo.2002.08.001

Ramos-Scharrón, C. E., & Arima, E. (2019). Hurricane María's Precipitation Signature in Puerto Rico: A Conceivable Presage of Rains to Come. *Scientific Reports*, *9*(1). https://doi.org/10.1038/s41598-019-52198-2

Regmi, N. R., Giardino, J. R., & Vitek, J. D. (2014). Characteristics of landslides in western Colorado, USA. *Landslides*, *11*(4), 589–603. https://doi.org/10.1007/s10346-013-0412-6

Reid, H. F., & Taber, S. (1918). The Bulletin of the Seismological Society of America. In *Bull. Seis. Soc. Am: Vol. I X* (Issue 7).

Roda-Boluda, D. C., D'Arcy, M., McDonald, J., & Whittaker, A. C. (2018). Lithological controls on hillslope sediment supply: insights from landslide activity and grain size distributions. *Earth Surface Processes and Landforms*, *43*(5), 956–977. https://doi.org/10.1002/esp.4281

Rogers, C. L., Cram, C. M., Pease Jr., M. H., & Tischler, M. S. (1979). *Geologic Map of the Yabucoa and Punta Tuna Quadrangles, Puerto Rico*.

Sassa, K., & Canuti, P. (2009). *Disaster Risk Reduction*. Springer Verlag.

Schulz, W. H. (2007). *Landslide susceptibility revealed by LIDAR imagery and historical records , Seattle , Washington ☆*. *89*, 67–87. https://doi.org/10.1016/j.enggeo.2006.09.019

Shiels, A. B., & Walker, L. A. (2013). Landslides cause spatial and temporal gradients at multiple scales in the Luquillo Mountains of Puerto Rico. *Ecological Bulletins 54: Ecological Gradient Analyses in a Tropical Landscape*, *54*, 211{\textendash}221. https://www.aphis.usda.gov/wildlife_damage/nwrc/publications/13pubs/shiels134.pdf

Silva-Tulla, F., A. Pando, M., Pradel, D., Park, Y., & Kayen, R. (2020). Geotechnical Consequences and Failures in Puerto Rico Due to Hurricane Maria. *Geo-Congress*, *1*(Shin 2005), 640–648.

Silverman, B. W. (1984). Spline Smoothing : The Equivalent Variable Kernel Method Author (s): B . W . Silverman Source : The Annals of Statistics , Vol . 12 , No . 3 (Sep ., 1984), pp . 898-916 Published by : Institute of Mathematical Statistics Stable URL : http://www.jstor. *The Annals of Statistics*, *12*(3), 898–916.

Struck, M., Andermann, C., Hovius, N., Korup, O., Turowski, J. M., Bista, R., Pandit, H. P., & Dahal, R. K. (2015). Monsoonal hillslope processes determine grain size-specific suspended sediment fluxes in a trans-Himalayan river. *Geophysical Research Letters*, *42*(7), 2302–2308. https://doi.org/10.1002/2015GL063360

Tron, S., Dani, A., Laio, F., Preti, F., & Ridolfi, L. (2014). Mean root depth estimation at landslide slopes. *Ecological Engineering*, *69*, 118–125. https://doi.org/10.1016/j.ecoleng.2014.03.019

Turner, B. F., Stallard, R. F., & Brantley, S. L. (2003). Investigation of in situ weathering of quartz diorite bedrock in the Rio Icacos basin, Luquillo experimental forest, Puerto Rico. *Chemical Geology*, *202*(3–4), 313–341. https://doi.org/10.1016/j.chemgeo.2003.05.001

USGS National Map. (2020). *USGS National Map*. https://viewer.nationalmap.gov/basic/

Varnes, D. (1978). Slope Movement Types and Processes. *Special Report*, *176*, 11–33.

White, A. F., & Blum, A. E. (1995). Effects of climate on chemical, weathering in watersheds. In *Pergamon Geochimica et Cosmochimica Acta* (Vol. 59, Issue 9).

White, A. F., Blum, A. E., Schulz, M. S., Bullen, T. D., Harden, J. W., & Peterson, M. L. (1996). Chemical Weathering of a Soil Chronosequence on Granite Alluvium I. Reaction Rates Based on Changes in Soil Mineralogy. *Geochimica et Cosmochimica Acta*, *60*(14), 2533–2550.

White, A. F., Blum, A. E., Schulz, M. S., Vivit, D. V., Stonestrom, D. A., Larsen, M., Murphy, S. F., & Eberl, D. (1998). Chemical weathering in a tropical watershed, Luquillo Mountains, Puerto Rico: I. Long-term versus short-term weathering fluxes. *Geochimica et Cosmochimica Acta*. https://doi.org/10.1016/S0016-7037(97)00335-9

White, A. F., Bullen, T. D., Vivit, D. V., Schulz, M. S., & Clow, D. W. (1999). The role of disseminated calcite in the chemical weathering of granitoid rocks. *Geochimica et Cosmochimica Acta*. https://doi.org/10.1016/S0016-7037(99)00082-4